
Research Articles: Neurobiology of Disease

Depressed Synaptic Transmission and Reduced Vesicle Release Sites in Huntington's Disease Neuromuscular Junctions

Ahmad Khedraki^{1,3}, Eric J. Reed¹, Shannon H. Romer¹, Qingbo Wang², William Romine¹, Mark M. Rich², Robert J. Talmadge³ and Andrew A. Voss¹

¹Department of Biological Sciences, Wright State University, Dayton, OH 45435

²Department of Neuroscience, Cell Biology & Physiology, Wright State University, Dayton, OH 45435

³California State Polytechnic University, Pomona, Department of Biological Sciences, Pomona, CA, 91768

DOI: 10.1523/JNEUROSCI.0313-17.2017

Received: 2 February 2017

Revised: 6 July 2017

Accepted: 11 July 2017

Published: 19 July 2017

Author contributions: A.K., E.J.R., S.H.R., Q.W., R.J.T., and A.A.V. performed research; A.K., E.J.R., S.H.R., W.R., M.M.R., R.J.T., and A.A.V. analyzed data; A.K., E.J.R., S.H.R., W.R., M.M.R., R.J.T., and A.A.V. wrote the paper; S.H.R., M.M.R., R.J.T., and A.A.V. designed research.

Conflict of Interest: The authors declare no competing financial interests.

We thank Mrs. Lori Goss for surgical assistance with the denervation studies, Dr. Kevin Novak for work with the extensor digitorum longus muscle, Mr. Stephen Burke for assistance with the levator auris longus dissections, and Dr. Xueyong Wang for technical advice. Postnatal day 1 muscle samples were kindly provided by Dr. Theodore Garland, Jr. of the University of California, Riverside. This work was supported by NIH/NIGMS grant 1SC3GM096945 and Wright State University startup funds (AAV) as well as NIH/NINDS grant R01082354 (MMR).

Correspondence to Andrew A. Voss, Wright State University, 235 Biological Sciences, 3640 Colonel Glenn Hwy, Dayton, OH 45435, USA, 937-775-3734., Email: andrew.voss@wright.edu

Cite as: J. Neurosci ; 10.1523/JNEUROSCI.0313-17.2017

Alerts: Sign up at www.jneurosci.org/cgi/alerts to receive customized email alerts when the fully formatted version of this article is published.

Accepted manuscripts are peer-reviewed but have not been through the copyediting, formatting, or proofreading process.

Copyright © 2017 the authors

1 **Depressed Synaptic Transmission and Reduced Vesicle Release Sites in Huntington's**

2 **Disease Neuromuscular Junctions**

3 **Abbreviated title:** Neuromuscular Transmission in Huntington's disease

4 **Authors:** Ahmad Khedraki^{1,3}, Eric J. Reed¹, Shannon H. Romer¹, Qingbo Wang², William

5 Romine¹, Mark M. Rich², Robert J. Talmadge³, and Andrew A. Voss¹

6 ¹Department of Biological Sciences, Wright State University, Dayton, OH 45435

7 ²Department of Neuroscience, Cell Biology & Physiology, Wright State University, Dayton, OH

8 45435

9 ³California State Polytechnic University, Pomona, Department of Biological Sciences, Pomona,

10 CA, 91768

11 Correspondence to Andrew A. Voss, Wright State University, 235 Biological Sciences, 3640

12 Colonel Glenn Hwy, Dayton, OH 45435, USA, 937-775-3734.

13 Email: andrew.voss@wright.edu

14 **Number of Pages: 35 with no figure legends and 39 with figure legends**

15 **Number of Figures: 11 and Tables: 1**

16 **Number of words for Abstract: 224, Introduction: 649, and Discussion: 1,483**

17 **Conflict of Interest**

18 The authors declare no competing financial interests.

19 **Acknowledgements**

20 We thank Mrs. Lori Goss for surgical assistance with the denervation studies, Dr. Kevin Novak

21 for work with the extensor digitorum longus muscle, Mr. Stephen Burke for assistance with the

22 levator auris longus dissections, and Dr. Xueyong Wang for technical advice. Postnatal day 1

23 muscle samples were kindly provided by Dr. Theodore Garland, Jr. of the University of

24 California, Riverside. This work was supported by NIH/NIGMS grant 1SC3GM096945 and

25 Wright State University startup funds (AAV) as well as NIH/NINDS grant R01082354 (MMR).

26 **ABSTRACT**

27 Huntington's disease (HD) is a progressive and fatal degenerative disorder that results in
28 debilitating cognitive and motor dysfunction. Most HD studies have focused on degeneration of
29 the central nervous system. We previously discovered that skeletal muscle from transgenic R6/2
30 HD mice is hyperexcitable due to decreased chloride and potassium conductances. The
31 progressive and early onset of these defects suggest a primary myopathy in HD. In this study,
32 we examined the relationship between neuromuscular transmission and skeletal muscle
33 hyperexcitability. We used an *ex vivo* preparation of the levator auris longus muscle from male
34 and female late-stage R6/2 mice and age-matched wild-type controls. Immunostaining of the
35 synapses and molecular analyses revealed no evidence of denervation. Physiologically, we
36 recorded spontaneous miniature endplate currents (mEPCs) and nerve-evoked endplate
37 currents (eEPCs) under voltage clamp, which, unlike current clamp records, were independent
38 of the changes in muscle membrane properties. We found a reduction in the number of vesicles
39 released per action potential (quantal content) in R6/2 muscle, which analysis of eEPC variance
40 and morphology indicate is caused by a reduction in the number of vesicle release sites (n)
41 rather than a change in the probability of release (p_{rel}). Furthermore, analysis of high frequency
42 stimulation trains suggests an impairment in vesicle mobilization. The depressed neuromuscular
43 transmission in R6/2 muscle may help compensate for the muscle hyperexcitability and
44 contribute to motor impersistence.

45

46 **SIGNIFICANCE STATEMENT**

47 Recent evidence indicates that Huntington's disease (HD) is a multi-system disorder. Our
48 examination of neuromuscular transmission in this study reveals defects in the motor nerve
49 terminal that may compensate for the muscle hyperexcitability in HD. The technique we used
50 eliminates the effects of the altered muscle membrane properties on synaptic currents and thus
51 provides hitherto the most detailed analysis of synaptic transmission in HD. Clinically, the

- 52 striking depression of neurotransmission we found may help explain the motor impersistence in
- 53 HD patients. Therapies that target the highly accessible peripheral nerve and muscle system
- 54 provide a promising new avenue to lessen the debilitating motor symptoms of HD.

55 **INTRODUCTION**

56 Huntington's disease (HD) is a fatal degenerative disorder that is characterized by
57 severe affective, cognitive, and behavioral psychiatric abnormalities, as well as numerous motor
58 defects, including chorea, rigidity, dystonia, and bradykinesia (Wells and Ashizawa, 2006). It is
59 caused by an expanded CAG trinucleotide repeat in exon 1 of the *huntingtin* gene (Group,
60 1993) and is one of several trinucleotide repeat disorders (Wells and Ashizawa, 2006). Although
61 the *huntingtin* gene is widely expressed throughout the body, including skeletal muscle, most
62 research on the disease has focused on the central nervous system (Group, 1993; Strand et al.,
63 2005; Wells and Ashizawa, 2006; Lo and Hughes, 2010). Neurodegeneration in the striatum
64 and cortex have been widely assumed to underlie the severe motor defects of HD (Strand et al.,
65 2005; Wells and Ashizawa, 2006). However, the expression of mutated *huntingtin* in the skeletal
66 muscle could cause muscle dysfunction independent of neurodegeneration.

67 In support of primary muscle defects, motor symptoms were shown to precede the onset
68 of neurological symptoms in a marathon runner with HD (Kosinski et al., 2007). Moreover, a
69 number of studies have demonstrated pathological changes in HD muscle, including metabolic
70 and mitochondrial defects (Lodi et al., 2000; Turner et al., 2007; Mielcarek et al., 2015), atrophy
71 (Ribchester et al., 2004; She et al., 2011; Ehrnhoefer et al., 2014), reduced muscle strength
72 (Busse et al., 2008; Hering et al., 2016), and a reduced expression of genes necessary for
73 normal muscle differentiation (Luthi-Carter et al., 2002; Strand et al., 2005). Additionally, we
74 previously discovered that skeletal muscle from R6/2 transgenic HD mice is hyperexcitable due
75 to decreased currents through chloride (ClC-1) and inwardly rectifying potassium (Kir) channels,
76 which correlated with aberrant mRNA processing and lower levels of mature full-length mRNAs
77 for ClC-1 and Kir channels (Waters et al., 2013). We further showed that these muscle defects
78 begin in presymptomatic R6/2 mice, increase in parallel to disease progression, and are
79 associated with disruptions in muscle maturation (Miranda et al., 2017).

80 It is also possible that defects in motor neurons could contribute to HD symptoms. It has
81 been shown that motor neurons in the brainstem of wildtype (CD1) mice increase expression
82 the *huntingtin* gene through development into adulthood (Bhide et al., 1996). Other papers have
83 speculated changes in HD spinal motor neurons (Ribchester et al., 2004; Mielcarek et al., 2015)
84 and a recent study reported smaller and fewer cervical spinal motor neurons with atypical nuclei
85 in the BACHD mice (Valadao et al., 2017).

86 In this report, we begin to examine the relationship between muscle and neuronal
87 defects in HD. To determine if denervation or motor unit loss drives the HD skeletal muscle
88 hyperexcitability, as proposed in a study based on contraction experiments (Mielcarek et al.,
89 2015), we examined neuromuscular morphology and the expression levels of key molecular
90 markers for denervation in R6/2 mice. Our main focus in this report was to measure
91 neuromuscular transmission under voltage clamp conditions. This is important because the
92 standard corrections used to account for nonlinear summation in current clamp recordings of
93 synaptic potentials (McLachlan and Martin, 1981) would not account for the changes in the R6/2
94 muscle membrane properties that cause hyperexcitability. Most of the previous studies of
95 neuromuscular transmission in HD used current clamp (Ribchester et al., 2004; Romero et al.,
96 2008; Rozas et al., 2011; de Aragao et al., 2016) and were completed before we reported that
97 R6/2 muscle is hyperexcitable and has a lower specific membrane capacitance.

98 We found that muscle hyperexcitability in R6/2 mice was not driven by denervation.
99 However, despite the normal appearance of the neuromuscular junctions, we did find evidence
100 of fewer functional active sites and impaired vesicle release in R6/2 mice, both of which may
101 help compensate for the muscle hyperexcitability. We also show that the changes in R6/2
102 muscle membrane properties alter corrected synaptic potentials measured under current clamp,
103 which has experimental implications for many studies of synaptic transmission in disease states.
104

105 **MATERIALS AND METHODS**106 **Animal Care**

107 All animal procedures were performed in accordance with the policies of the Animal
108 Care and Use Committee of Wright State University. We established a breeding colony in the
109 Wright State University Laboratory Animal Resources (LAR) Facility that consisted of one wild
110 type B6CBA female with an ovarian transplant (hemizygous for Tg(HDexon1)62Gpb) and one
111 wild type male (B6CBAF1/J) purchased from The Jackson Laboratory (Bar Harbor, ME), stock
112 number 002810 (RRID: IMSR_JAX:002810, <https://www.jax.org/strain/002810>). A total of 40
113 male and female R6/2 and 52 male and female control mice produced from 12 breeding pairs
114 were used for this study. Tail samples cut between 7 and 14 days of age were genotyped at
115 Laragen Inc. (Culver City, CA). Mice were housed with wild type littermates in sex-matched
116 cages after weaning at roughly 14 days of age. Beginning at 9 weeks of age, all cages housing
117 R6/2 mice were supplied with a Petri dish containing moist chow (dry chow soaked in water) to
118 ensure adequate nutritional intake in the symptomatic mice.

119 Health and phenotype severity assessment for HD mice, as described previously
120 (Waters et al., 2013; Miranda et al., 2017), were performed weekly for mice 8 to 10 weeks of
121 age, every other day for mice 10 weeks of age, and daily for mice ≥ 11 weeks of age.
122 Assessment categories included physical condition, respiratory health, activity level, and weight
123 loss. Mice were rated on a scale from 0 to 3 for each category, where 0 signified a normal
124 condition and 3 signified a severe/poor condition. Mice were selected for experiments when the
125 sum of all the category scores was ≥ 6 or when the score of any one category equaled 3. Of the
126 behavioral measures, mouse weight has been a reliable and easy to assess measure of
127 disease progression. We previously showed that R6/2 weight stopped increasing from 6 – 10
128 weeks of age and decreased after 10 weeks of age (Miranda et al., 2017). Experiment-ready
129 mice were euthanized by inhalation of a saturating dose of isoflurane ($\sim 2\text{g/L}$), followed by

130 cervical dislocation. All R6/2 and control mice used in this study were between 11 and 14 weeks
131 of age.

132 For denervation studies, SWR/J mice were anesthetized with inhaled isoflurane. The
133 region of the left sciatic notch was shaved and sterilized, an incision was made and a 3 mm
134 length of the sciatic nerve was removed. The wound was closed with sutures and mice were
135 allowed to recover. One week later mice were euthanized with inhaled CO₂ and the right and left
136 gastrocnemius muscles were removed and flash frozen in liquid nitrogen.

137

138 **Electrophysiology**

139 The levator auris longus (LAL) muscle was dissected from the mice and pinned to a
140 custom Sylgard perfusion chamber. Muscle fibers were visualized using an Olympus BX51WI
141 microscope equipped with 10x (UMPLFLN10XW) and 40x (LUMPLFLN40XW) objectives. The
142 extracellular buffer solution consisted of (in mM): 144 NaCl, 4 KCl, 1.2 CaCl₂, 0.6 MgCl₂, 5
143 glucose, 1 NaH₂PO₄, 10 MOPS, and pH 7.4 with NaOH. A low Ca²⁺ extracellular buffer was also
144 used and consisted of (in mM): 140 NaCl, 4 KCl, 0.5 CaCl₂, 4 MgCl₂, 5 glucose, 1 NaH₂PO₄, 10
145 MOPS, and pH 7.4 with NaOH. Both the normal and low Ca²⁺ buffers had an osmolality of 300 ±
146 5 mmol/kg. To prevent muscle contraction during nerve stimulation, 60 μM N-benzyl-p-toluene
147 sulphonamide (BTS) and 1 μM μ-conotoxin GIIIB (in normal Ca²⁺ only) were used. To visualize
148 neuromuscular junctions (NMJs), fibers were stained with 5 μM 4-(4-diethylaminostyryl)-N-
149 methylpyridinium iodide (4-Di-2-ASP) for 5 minutes. 4-Di-2-ASP is a cationic fluorescent
150 mitochondrial dye that stains presynaptic nerve terminals with no lasting effects on their
151 structure or function (Magrassi et al., 1987). A Thorlabs M470L3 collimated LED (470 nm) or
152 halogen bulb and an eGFP filter cube were used to observe fluorescence. Solution changes
153 were achieved via a custom gravity-driven perfusion system and all experiments were
154 performed at room temperature (22°C).

155 Fibers within the rostral band of the LAL were impaled using two borosilicate glass
156 microelectrodes (Sutter Instruments, Novato, CA) positioned within 100 μm of one another and
157 within 100 μm of the NMJ to obtain proper space clamp of the endplate region (Albuquerque
158 and Mclsaac, 1970). The distance of electrodes from one another and from the NMJ were
159 measured with ImageJ (National Institutes of Health) from images acquired with a Santa
160 Barbara Instruments Group (SBIG) ST-7XMEI CCD camera (SBIG, Goleta, CA). The internal
161 solution used for the voltage-reading electrode was 3M KCl and the internal solution of the
162 current-passing electrode consisted of (in mM): 75 aspartate, 5 MgCl_2 , 15 $\text{Ca}(\text{OH})_2$, 5 ATP
163 disodium, 5 phosphocreatine disodium, 5 glutathione, 20 MOPS, 30 EGTA, pH 7.2 with KOH,
164 and osmolality of 300 ± 5 mmol/kg. All electrode resistances were between 10 and 15 $\text{M}\Omega$. An
165 Axoclamp 900A amplifier, Digidata 1550 digitizer, and the pCLAMP 10 data acquisition and
166 analysis software (Molecular Devices, Sunnyvale, CA) were used for synaptic current and
167 voltage clamp recordings. Nerve stimulation was achieved using a Master-9 Pulse Generator
168 and an ISO-Flex stimulus isolator (A.M.P.I., Jerusalem, Israel) in conjunction with a CBDSH75
169 concentric bipolar electrode (FHC, Bowdoin, ME) that was positioned directly onto the nerve
170 using a small Narshige ball-joint manipulator.

171 Fibers with high miniature endplate potential (mEPP) or miniature endplate current
172 (mEPC) frequency ($>3\text{Hz}$ in physiological Ca^{2+} and $>4\text{Hz}$ in low Ca^{2+}) were discarded to avoid
173 studying potentially damaged nerve terminals. Fibers necessitating more than -25 nA of holding
174 current to maintain the membrane potential between -80 and -90 mV were also discarded.
175 Prior to entering voltage clamp, an equal number of small positive and negative square current
176 pulses (between -14 and $+14$ nA) were injected under current clamp to determine the
177 membrane time constant (τ_m).

178 The motor endplates were voltage-clamped to -85 mV. Achieving adequate voltage
179 control can be a concern. As described above, electrodes were impaled at distances from the
180 NMJ that were within the muscle length constant. Additionally, we used the DC restore feature

181 of the Axoclamp 900A, which sets a very high voltage clamp gain (~1,000,000). Under these
182 conditions, the entire motor endplate was clamped at the holding potential (-85 mV). Even
183 under these conditions, however, the voltage clamp gain and lag settings influence the rate at
184 which the amplifier will maintain the holding potential – fast currents may cause a momentary
185 voltage deflection. Moreover, resolving mEPCs from noise required lower gain and lag settings
186 than we previously used to voltage clamp whole flexor digitorum brevis fibers (Waters et al.,
187 2013; Miranda et al., 2017). To assess our voltage clamp, we measured the voltage deflection
188 that occurred during nerve-evoked endplate currents (eEPCs) in 5 WT and R6/2 fibers (10 per
189 fiber). These data were representative of mean eEPC values. The average voltage deflections
190 during the peak eEPC in the WT and R6/2 fibers was only 1.4 ± 0.3 mV and 0.8 ± 0.2 mV,
191 respectively. Moreover, by integrating the full mEPCs and eEPCs to obtain the total charge, we
192 minimized the contribution of the voltage deflection. To estimate the amount of charge
193 attributable to the voltage deflections, we converted the voltage signal to current (deflection
194 current) using the fiber input resistance (obtained under current clamp from the same fibers).
195 We then integrated the deflection current over the time course of the corresponding eEPCs to
196 obtain the deflection charge. The | deflection charge | / | eEPC charge | ratio was $3.9 \times 10^{-4} \pm$
197 1.3×10^{-4} and $1.1 \times 10^{-4} \pm 4.0 \times 10^{-5}$ for WT and R6/2 and plates, respectively. Thus, based on
198 this ratio, the percentage of unclamped endplate in our experiments was <0.05%. Voltage
199 clamp settings (Gain: 1500, Lag: 1, and pipette capacitance neutralized) were maintained the
200 same across all fibers. To estimate the quantal content (QC), the nerve was stimulated at 0.5
201 Hz with the stimulus intensity set to 1.5-2X the threshold required to elicit an eEPC and we
202 recorded the resulting eEPCs and spontaneously occurring mEPCs for 2 minutes. The same
203 protocol was used for low calcium experiments. QC was calculated using the equation below.

$$(1) \quad QC = \frac{\text{mean eEPC charge}}{\text{mean mEPC charge}}$$

204 To estimate of the probability of synaptic release (p_{rel}) and the number of available

205 release sites (n), we used a graphical approach based on binomial vesicle release statistics
 206 (Clements and Silver, 2000; Wang et al., 2010). QC was calculated using equation (1) and the
 207 variance of QC ($\text{Var}(\text{QC})$) was calculated with the equation below.

$$208 \quad (2) \quad \text{Var}(\text{QC}) = \left(\frac{\text{standard deviation of peak eEPC amplitude}}{\text{mean of peak mEPC amplitude}} \right)^2$$

209 We assumed the following relationships.

$$(3) \quad \text{QC} = np$$

$$(4) \quad \text{Var}(\text{QC}) = np(1 - p)$$

210 To estimate n from $\text{Var}(\text{QC})$ vs. QC plots, we substituted $p = \text{QC}/n$, a rearranged form of
 211 equation (3), into equation (4) to obtain the parabola equation below.

$$(5) \quad \text{Var}(\text{QC}) = \text{QC} \left(1 - \frac{\text{QC}}{n} \right)$$

212 For high frequency stimulation, the nerve was stimulated at 50 Hz during 200 ms trains
 213 (10 eEPCs). Each fiber was stimulated with 10 such trains with a 10 second pause between
 214 each train. To assess depression in normal Ca^{2+} , the peak amplitude of each eEPC was
 215 normalized to the peak amplitude of the largest eEPC in the train. We also used the degree of
 216 depression to compare depression severity, determined by dividing the amplitude of the last
 217 eEPC by the first eEPC in a train. In all protocols, acquisition rate was set to 20 KHz and signals
 218 were low-pass filtered at 1 KHz.

219 To determine the effects of the altered muscle membrane properties on corrected
 220 synaptic potentials recorded under current clamp, we applied the 0.5 Hz stimulation protocol
 221 described above to a subset of the fibers under both voltage clamp and current clamp. We
 222 corrected the miniature endplate potentials (mEPPs) and evoked endplate potentials (eEPPs)
 223 recorded under current clamp for differences in resting membrane potential and nonlinear
 224 summation as described previously for R6/1 HD mice (Rozas et al., 2011), which was based on
 225 work by McLachlan and Martin, 1981. Briefly, end plate potentials were normalized for changes

226 in resting membrane potential ($mEPP_{norm}$ and $eEPP_{norm}$) using $mEPP_{norm} = mEPP(-75/V_m)$
227 and $eEPP_{norm} = eEPP(-75/V_m)$, where V_m is the resting membrane potential. To correct the
228 evoked endplate potentials for nonlinear summation, we used
229 $eEPP_{corr} = eEPP_{norm}/[1 - 0.8(eEPP_{norm}/E)]$, where E is the difference between V_m and the
230 equilibrium potential for current through the nicotinic acetylcholine receptor (nAChR). As was
231 done previously (Rozas et al., 2011), we assumed the equilibrium potential for nAChR currents
232 was 0 mV. QC using current clamp (QC_{IC}) data was obtained from
233 $QC_{IC} = \text{mean } eEPP_{corr} / \text{mean } mEPP_{norm}$.

234 Resting membrane potential measurements were obtained from extensor digitorum
235 longus fibers as previously described (Novak et al., 2015). Briefly, muscle samples were
236 examined under an upright epifluorescence microscope (Leica DMR, Bannockburn, IL) and
237 continuously perfused with a recirculating Ringer solution containing (in mM), 118 NaCl, 3.5
238 KCl, 2 CaCl₂, 0.7 MgSO₄, 26.2 NaHCO₃, 1.7 NaH₂PO₄, 5.5 glucose, and equilibrated with 95%
239 O₂ and 5% CO₂ to maintain the pH 7.3–7.4 at 20–22°C. Fibers were impaled with single sharp
240 microelectrodes to minimize membrane damage. The electrodes were filled with 3M KCl and 1
241 mM sulforhodamine (for visualization) and had resistances between 15 and 30 MΩ. Resting
242 membrane potential records were acquired using a Geneclamp 500B amplifier (Axon
243 Instruments) as well as a Power 1401 data acquisition board and Spike2, version 5.13 software
244 (Cambridge Electronics Design, Cambridge, UK). The initial membrane potential upon impaling
245 the electrode was considered the resting membrane potential.

246

247 **Immunostaining**

248 To assess innervation, whole mount LAL muscles were dissected and pinned out in
249 Sylgard dishes, fixed for 15 minutes with 4% paraformaldehyde in phosphate buffered saline
250 (PBS), and washed three times for 10 minutes with PBS. To identify the postsynaptic side of
251 NMJs, we labeled nAChRs with a 30-minute exposure to solution containing 20 µg/ml of

252 rhodamine-conjugated α -bungarotoxin (Molecular Probes, Carlsbad, CA, USA). To label
253 presynaptic nerve terminals, we stained the LAL for neurofilaments with monoclonal anti-mouse
254 antibody directed against SMI 31 (Covance Research Products, Princeton, NJ, 1:500 dilution)
255 and for presynaptic vesicles with the monoclonal anti-mouse antibody against SV2
256 (AB_2315387, Developmental Studies Hybridoma Bank, University of Iowa, 1 μ g/ml). The LAL
257 was exposed to both primary antibodies overnight at 4 °C. A 2-hour room temperature
258 incubation with secondary fluorescein-conjugated anti-mouse antibody (Jackson
259 ImmunoResearch Laboratories) was used to label both neurofilament and presynaptic vesicle
260 primary antibodies. The whole mount LAL was then washed 3 times in PBS and mounted using
261 Vectashield (Vector Laboratories). We used an Olympus FV 1000 confocal microscope with a
262 60x oil immersion objective (N.A. 1.4) to image the endplates. Stained sections were analyzed
263 using Olympus Fluoview software.

264 Quantification of NMJ morphology and bassoon localization was completed in dissected,
265 whole mount R6/2 and control LAL muscles that were pinned out in a Sylgard dish and fixed
266 with 4% paraformaldehyde in PBS for 1 hour. The fixed LAL samples were washed in PBS,
267 rinsed with PBS-T (0.01M PBS containing 0.3% Triton-X, pH 7.3), and blocked with normal
268 horse serum (10% in PBS-T) for 1 hour. Samples were immunostained free-floating in 12-well
269 plates. Primary and secondary antibodies were diluted in PBS-T with 10% normal horse serum.
270 To detect presynaptic active zones, muscle tissue was incubated in mouse anti-bassoon
271 antibody (Abcam AB82958 Lot GR78505, 1:1000 dilution) overnight at 4°C. Immunoreactivity
272 (IR) was detected with Alexa 488 conjugated donkey anti-mouse antibody (Jackson Immuno,
273 West Grove, PA, USA; 1:250 dilution) for 2 hours at room temperature with gentle shaking. To
274 detect postsynaptic membrane, muscle tissue was incubated in Alexa 555-conjugated α -
275 bungarotoxin (Molecular Probes, Carlsbad, CA, USA, 1:1000 dilution) for 20 minutes. Tissue

276 was washed and mounted on charged microslides in Vectashield mounting medium (Vector,
277 Burlingame, CA, USA) and coverslipped.

278 Approximately 12 *enface* NMJs were randomly selected and imaged on a Fluoview 1000
279 Olympus (Center Valley, PA) confocal microscope with a 60x objective (N.A. 1.35 oil) with 2.5x
280 zoom at 0.3 μ m Z-steps through the entire NMJ. Confocal stacks were superimposed and
281 flattened in Fluoview software (Olympus, Center Valley, PA) and TIFFs analyzed in Image Pro
282 Software (Media Cybernetics, Silver Springs, MD, USA). Two complimentary features of Image
283 Pro Software were used to quantify colocalization of the bassoon-IR to α -bungarotoxin-Alexa 555,
284 in: 1) the colocalization coefficient, which estimates the contribution of one channel color
285 (bassoon green-IR) to the overall colocalized fluorescence of the region of interest, and 2) the
286 overlap coefficient of colocalization, which quantitates the overlap of the two colors. These
287 methods are not sensitive to intensity variations in the image analysis. Quantification was
288 always carried out in original unprocessed images. Microscope images were prepared by
289 adjusting contrast and brightness in Image Pro Plus Software (Media Cybernetics, Bethesda,
290 MD, USA), with all information content of the images being preserved. Figures were composed
291 using CorelDraw (v. 12.0). Graphs were composed in SigmaPlot 13 software (Systat Software,
292 San Jose, CA). Some images were sharpened using a "high gauss" filter in Image Pro.

293

294 **mRNA analysis**

295 Tibialis anterior, soleus and LAL muscles were removed from R6/2 and control mice, snap
296 frozen in liquid nitrogen, and stored at -80°C until analyzed. Total RNA was isolated using
297 RNeasy kits (Qiagen Sciences, Valencia, CA) and RNA stored at -80°C . Reverse
298 transcriptase-polymerase chain reaction (RT-PCR) methods were used for the quantification of
299 the following denervation-induced mRNAs: 1) the γ -subunit of nAChR (nAChR γ) (Moss et al.,
300 1987; Witzemann et al., 1987; Gu and Hall, 1988a, b; Adams et al., 1995; Liu et al., 2016); 2)

301 the small-conductance calcium-activated potassium channel (SK3) (Pribnow et al., 1999;
302 Neelands et al., 2001; Jacobson et al., 2002; Favero et al., 2008); and 3) the cardiac muscle
303 isoform of the voltage-gated sodium channel, Nav1.5 (Scn5a) (Rogart et al., 1989; Lupa et al.,
304 1995; Sekiguchi et al., 2012). Reverse transcription was performed using Superscript III reverse
305 transcriptase and random primers according to the manufacturer's instructions (Invitrogen). The
306 levels of nAChR γ mRNA were evaluated in two ways. First, a gel-based PCR method utilizing
307 primers flanking the following genes, nAChR γ (upstream: 5'-GGGCCGAGTGCTGGACCG-3',
308 downstream: 5'-GGCGGGGTCTCCGGGA-3') and SK3 (upstream: 5'-
309 CAAGTGTCCCTGTCCATCTTC-3', downstream: 5'-CCAAGTGGTCATTGAGATTTA-3'). The
310 18S ribosomal subunit was also quantified via RT-PCR for control purposes with primers from
311 Ambion. Second, the same nAChR γ primers were used for the relative quantification of nAChR γ
312 in a real-time Sybr Green-based RT-PCR (qPCR) procedure using the Full Velocity™ SYBR®
313 green kit (Stratagene). The mRNA levels of SK3 were quantified in a similar manner. The
314 mRNA levels of Scn5a were quantified using a TaqMan® based assay (Mm01342518.m1,
315 Applied Biosystems). RNA from 14-day denervated and control mouse gastrocnemius muscles
316 and hindlimb muscle from postnatal day 1 mice were used as positive controls for denervation-
317 induction (and developmental expression) of the denervation-sensitive genes. For real-time RT-
318 PCR quantification, the cycle thresholds were obtained for β -2-microglobulin as a normalizing
319 gene using a TaqMan® based assay (Mn00437762.m1, Applied Biosystems). The $\Delta\Delta$ CT
320 method was used for calculation of relative expression levels (Livak and Schmittgen, 2011).

321

322 **Statistics**

323 The means of two normal sample populations, as per the Shapiro-Wilk test, were
324 compared using a two-tailed Student's t-test using SigmaPlot 13 software (Systat Software, San
325 Jose, CA). Any non-normal sample population means were compared using the Mann-Whitney

326 rank sum test. Mean values were reported as mean \pm SEM. A one-way ANCOVA model
327 generated with Stata (College Station, TX) was used to evaluate normalized eEPC charges
328 relative to position on the 0.5 Hz train for control and R6/2 groups, as well as between-group
329 differences between the trends. We evaluated the position along the domain of eEPCs #5-60 in
330 the train, which we centered at 0 for the analysis. This model can be expressed in terms of the
331 General Linear Model (GLM) equation:

$$332 \quad (6) \quad eEPC = b_0 + b_1Group + b_2Position + b_3Position \times Group + Error,$$

333 where b_0 represents eEPC charge of the control group at position = 5, b_1 represents the
334 difference between the control and R6/2 groups at position = 5, b_2 represents the average
335 change in eEPC charge per unit of position, and b_3 represents the difference in this rate of
336 change between the R6/2 and control groups. Significance of the regression model and each
337 parameter was evaluated at the 0.05 alpha level. Significance of b_0 indicates that the eEPC
338 charge for the control group at a position of 5 is significantly different from 0. A significant b_1
339 value indicates that the eEPC charge for the R6/2 group is significantly different from the control
340 group at this initial position. A significant b_2 value indicates that there is sufficient evidence to
341 detect a non-zero change in eEPC charge with respect to position for the control group, and a
342 significant b_3 value indicates that the rate of change for the R6/2 group is significantly different
343 from that in the control group. All p -values were calculated using the number of mice.

344 **RESULTS**345 **Skeletal muscle hyperexcitability**

346 Our previous work using two-electrode voltage clamp demonstrated that the flexor
347 digitorum brevis and interosseous muscles in R6/2 mice become hyperexcitable due to
348 decreases in the resting chloride and potassium currents early in the disease progression
349 (Waters et al., 2013; Miranda et al., 2017). Because of the reduced resting currents, the
350 membrane time constant (τ_m) of the R6/2 fibers was prolonged (Waters et al., 2013). Most of the
351 increase in τ_m was due to decreased currents through the muscle chloride channel, CIC-1,
352 which constitutes ~80% of the resting muscle conductance (Hutter and Noble, 1960; Steinmeyer
353 et al., 1991b; Steinmeyer et al., 1991a). To confirm that passive membrane properties were
354 similarly altered in the levator auris longus (LAL) muscle, we used current clamp to determine
355 the τ_m of late-stage R6/2 (4 male and 3 female mice, 81 fibers) and age-matched control fibers
356 from wild-type littermates (6 male and 4 female mice, 87 fibers); all mice were 11 – 14 weeks of
357 age (Fig. 1). These were the same motor endplates from which we measured neuromuscular
358 transmission in physiological extracellular Ca^{2+} in subsequent figures. We injected an equal
359 number of small positive and negative square current pulses into the motor endplate and
360 recorded the resulting changes in the membrane potential (Fig. 1A). The striking increase in
361 R6/2 fiber input resistance, indicated by the larger voltage responses, is known to occur
362 because of the combined effect of an increase in the membrane resistance (due to reduced
363 chloride and potassium conductance) and muscle fiber atrophy (Ribchester et al., 2004; Waters
364 et al., 2013). To eliminate the influence of atrophy, we measured the τ_m , which is independent of
365 fiber diameter, instead of the input resistance. To help ensure passive conditions, we estimated
366 the τ_m from the steady state voltage changes (ΔV) that were $< |5|$ mV and had linear voltage-
367 current relationships (Voss, 2009). We excluded values of ΔV that exceeded $|5|$ mV from our
368 τ_m calculations. τ_m was the time it took the membrane potential to reach $1/e$ of ΔV (~37% of the

369 steady state change in voltage) during the return to baseline after a current pulse. The τ_m of
370 R6/2 fibers (1.92 ± 0.06 ms) was significantly prolonged by 42% compared to that of control
371 (1.25 ± 0.07 ms, $p=5.94 \times 10^{-6}$, t-test where $t=6.805$ with 15 df), indicating that, consistent with
372 the R6/2 flexor digitorum brevis, the LAL muscle fibers we used to measure neuromuscular
373 transmission were hyperexcitable due to a loss of CIC-1 currents (Fig. 1B). The histogram in
374 Figure 1C shows a roughly normal distribution of R6/2 and control τ_m values, indicating that
375 R6/2 muscle fibers were uniformly hyperexcitable compared to control.

376

377 **Innervation**

378 To determine if the skeletal muscle fibers were anatomically denervated in late-stage
379 R6/2 mice (12-13 weeks old) compared to control (12-13 weeks old), we stained the nerve
380 terminals and motor endplates in whole mount LAL preparations (Fig. 2). Nerve terminals were
381 identified by staining for the neurofilaments and synaptic vesicles (both green). We identified the
382 motor endplates based on the binding of α -bungarotoxin-rhodamine (red) to nicotinic
383 acetylcholine receptors (nAChRs). In both control (276 neuromuscular junctions imaged from 3
384 mice) and R6/2 mice (274 neuromuscular junctions imaged from 3 mice), we found no
385 denervated endplates. This strongly suggests that the R6/2 skeletal muscle hyperexcitability
386 was not caused by denervation.

387 To further check for denervation, we tested for increased expression of the nAChR γ -
388 subunit (nAChR γ), which is expressed during development, repressed in adult muscle, and
389 upregulated following denervation (Hartzell and Fambrough, 1972; Lomo and Rosenthal, 1972;
390 Lomo and Westgaard, 1975; Moss et al., 1987; Witzemann et al., 1987; Gu and Hall, 1988a, b;
391 Adams et al., 1995; Kues et al., 1995; Liu et al., 2016). As shown in Figure 3A, neither R6/2 nor
392 control expressed nAChR γ mRNA at appreciable levels in the tibialis anterior (TA) or soleus
393 muscles. In contrast, the γ -subunit was readily detected in 14-day denervated mouse

394 gastrocnemius muscle but not in a contralateral control. We also detected nAChR γ in postnatal
395 day 1 hindlimb muscle (Fig. 3A). Furthermore, real-time RT-PCR (qPCR) assays demonstrated
396 that nAChR γ mRNA was not elevated in R6/2 mouse TA (Fig. 3B, control 1.000 ± 0.146 and
397 R6/2 0.745 ± 0.249 , $p=0.398$, t-test where $t=0.883$ with 10 df) or soleus (Fig. 3B, control $1.000 \pm$
398 0.503 and R6/2 0.321 ± 0.180 , $p=0.289$, t-test where $t=1.147$ with 7 df) muscle relative to
399 control. Molecular analyses of the TA were completed with 2 male and 4 female R6/2 mice as
400 well as 5 male and 1 female controls; one TA or soleus per mouse. For that of the soleus, each
401 RNA sample was a pool of two mouse solei of the indicated genotype without regard to sex. In
402 contrast to the R6/2 muscle, denervation of the mouse gastrocnemius (4 mice, each with
403 denervated sample and contralateral control) caused a significant elevation in the γ -subunit
404 mRNA (Fig. 3B, control 1.000 ± 0.623 and denervated 4.527 ± 0.717 , $p=0.010$, t-test where $t=-$
405 3.715 with 6 df). We also found that the levels of SK3 mRNA, which are upregulated following
406 denervation (Pribnow et al., 1999; Neelands et al., 2001; Jacobson et al., 2002; Favero et al.,
407 2008), were not significantly changed in the TA (control 1.000 ± 0.136 and R6/2 1.004 ± 0.229 ,
408 $p=0.991$, t-test where $t=-0.0115$ with 10 df) or soleus (control 1.000 ± 0.406 and R6/2 $0.563 \pm$
409 0.196 , $p=0.403$, t-test where $t=0.889$ with 7 df). As expected, denervation of the mouse
410 gastrocnemius caused a significant elevation in SK3 mRNA (control 1.000 ± 0.335 and
411 denervated 29.092 ± 3.566 , $p=2.0 \times 10^{-4}$, t-test where $t=-7.843$ with 6 df). The expression of
412 another positive marker for denervation, Scn5a, the cardiac isoform of the voltage gated sodium
413 channel (Rogart et al., 1989; Yang et al., 1991; Lupa et al., 1995; Rich et al., 1999; Sekiguchi et
414 al., 2012), was significantly reduced in the TA (control 1.000 ± 0.123 and R6/2 0.507 ± 0.141 ,
415 $p=0.025$, t-test where $t=2.630$ with 10 df) and unchanged in the soleus (control 1.000 ± 0.243
416 and R6/2 0.422 ± 0.130 , $p=0.094$, t-test where $t=1.934$ with 7 df) of R6/2 muscle. As shown for
417 the other denervation-sensitive genes, denervation of the mouse gastrocnemius caused a
418 significant elevation in Scn5a mRNA (Fig. 3B, control 1.000 ± 0.278 and denervated $44.209 \pm$

419 5.053, $p=1.0 \times 10^{-4}$, t-test where $t=-8.538$ with 6 df). There were also no molecular markers of
420 denervation in the LAL muscle. The same qPCR examination of control (2 male and 2 female
421 mice) and R6/2 LAL (1 male and 4 female mice) showed that nAChR γ (control 1.000 ± 0.446
422 and R6/2 0.572 ± 0.228 , $p=0.392$, t-test where $t=0.912$ with 7 df), SK3 (control 1.000 ± 0.288
423 and R6/2 0.554 ± 0.266 , $p=0.294$, t-test where $t=1.133$ with 7 df), and Scn5a (control $1.000 \pm$
424 0.467 vs R6/2 0.193 ± 0.085 , $p=0.097$, t-test where $t=1.914$ with 7 df) were not significantly
425 different.

426

427 **Neuromuscular transmission in low extracellular Ca²⁺**

428 Having determined that the hyperexcitability of R6/2 muscle fibers was independent of
429 denervation, we looked for changes in late-stage R6/2 neuromuscular transmission relative to
430 control. In *ex vivo* preparations of the LAL, we impaled two microelectrodes in rostral muscle
431 fibers and voltage clamped the motor endplate. Unlike the changes in muscle membrane
432 potential recorded under current clamp, voltage-clamped synaptic currents are independent of
433 the muscle membrane properties. In a reduced extracellular Ca²⁺ (0.5 mM) and elevated Mg²⁺ (4
434 mM) solution, we stimulated the motor nerve at 0.5 Hz and recorded evoked-endplate currents
435 (eEPCs) and spontaneous miniature-endplate currents (mEPCs) in control (3 male and 4 female
436 mice, 46 fibers) and R6/2 (4 male and 5 female mice, fibers 80) mice (Fig. 4A). The frequency of
437 mEPCs was significantly less in R6/2 (1.8 ± 0.3 Hz) than control (2.4 ± 0.2 Hz) NMJs ($p=0.02$, t-
438 test where $t=2.703$ with 14 df). Otherwise, we found no significant differences in mEPC charge
439 (control: -2.76 ± 0.13 pC, R6/2: -2.63 ± 0.07 pC, $p=0.38$, t-test where $t=-0.908$ with 14 df) or
440 eEPC charge (control: -3.73 ± 0.40 pC, R6/2: -4.52 ± 0.35 pC, $p=0.16$, t-test where $t=1.48$ with
441 14 df) at R6/2 NMJs compared to control (Fig. 4B). We also found no significant difference in
442 the quantal content (QC), which is the number of vesicles released per action potential (eEPC
443 charge/mEPC charge), at R6/2 NMJs (1.69 ± 0.10) compared to control (1.38 ± 0.16 , $p=0.11$, t-

444 test where $t=1.707$ with 14 df) (Fig. 4B). The findings in low Ca^{2+} suggest that synaptic
445 transmission was normal in R6/2 muscle.

446
447 **Neuromuscular transmission in physiological extracellular Ca^{2+}**

448 In order to obtain a more complete picture of neuromuscular transmission in R6/2
449 skeletal muscle, we measured endplate currents in physiological extracellular Ca^{2+} (1.2 mM)
450 and Mg^{2+} (0.6 mM) in the same fibers used to determine the membrane time constant. With
451 muscle contractions blocked using 1 μM $\mu\text{-CTX}$ and 60 μM N-benzyl-p-toluene sulphonamide
452 (BTS), we stimulated the motor nerve at 0.5 Hz and recorded eEPCs and mEPCs in control and
453 R6/2 mice for 2 min (Fig. 5A-D). The average mEPC frequency at R6/2 NMJs was significantly
454 lower than in controls (Table 1). Additionally, there were significant reductions in the average
455 R6/2 mEPC and eEPC charge compared to controls (Fig. 5E,F, Table 1). On average, R6/2
456 NMJs released 19% fewer vesicles per impulse than control terminals (QC in Fig. 5G, Table 1).
457 That the R6/2 mEPC and eEPC charge were not significantly different from control in low Ca^{2+}
458 suggests the defects in R6/2 neuromuscular transmission depend on Ca^{2+} . Thus, it seems
459 unlikely that impaired vesicle loading or the recently identified vesicle morphology changes (de
460 Aragao et al., 2016) could explain the reduced R6/2 mEPC and eEPC in physiological Ca^{2+} .

461 To determine if the lower QC in R6/2 NMJs was related to synaptic depression, we
462 examined the fractional amplitude of the eEPCs during the 0.5 Hz trains (Fig. 6A). The peak
463 amplitude of each eEPC was normalized to the peak of the largest eEPC in the train. Following
464 a transient initial depression, the fractional eEPC amplitudes in control NMJs appeared
465 unchanging or even slightly increasing; whereas, the eEPC amplitudes at R6/2 NMJs appeared
466 to depress slightly over the span of 60 stimulations (Fig. 6A). To assess the potential synaptic
467 modulation quantitatively, we examined eEPCs 5 – 60, which occurred after the initial transient
468 depression, with a General Linear Model. This model fit the data significantly better than using
469 the mean as a predictor ($F_{3,108}=125.5$, $p=4.6 \times 10^{-35}$, $r^2_{\text{adj}}=0.77$). Figure 6B shows the linear fit of

470 the normalized control and R6/2 eEPCs with 95% confidence intervals. The slight depression in
471 R6/2 eEPCs ($-5.2 \times 10^{-4} \pm 7.8 \times 10^{-5}$ EPC amplitude / nerve stimuli) was significantly different
472 from that of control ($2.6 \times 10^{-4} \pm 5.7 \times 10^{-5}$ eEPC amplitude / nerve stimuli; $b_3 = -7.8 \times 10^{-4}$,
473 $SE = 9.7 \times 10^{-5}$, $p = 1.4 \times 10^{-12}$, $t = -8.02$). To minimize the influence of this depression, we also
474 determined the QC based on eEPCs 5 – 24, which occurred after the transient depression and
475 early in the R6/2 depression. In this case, the R6/2 quantal content (53.9 ± 7.0) was still
476 significantly lower than control (64.8 ± 3.1 , $p = 0.022$, Mann-Whitney rank sum test where $U = 11$).
477 Furthermore, the R6/2 QC based only on the first eEPC (58.5 ± 1.9) was significantly less than
478 that of control (68.1 ± 3.3 ; $p = 0.0097$, Mann-Whitney rank sum test where $U = 8$).

479 We also analyzed the kinetics of mEPC and eEPC recorded in physiological Ca^{2+} and
480 Mg^{2+} (Fig. 7, Table 1). Figure 7 shows the average mEPC (Fig. 7A) and eEPC (Fig. 7B) from
481 representative control (solid lines) and R6/2 (dashed lines) fibers, each normalized to the peak.
482 The average rise and decay times of the R6/2 mEPCs and eEPCs were prolonged compared to
483 control (Fig. 7C,D, Table 1).

484 Understanding the contribution of changes in neuromuscular transmission to motor
485 function will be aided by knowing the resting membrane potential. Previous studies have shown
486 that the resting membrane potential of R6/2 muscle fibers was depolarized relative to control
487 (Ribchester et al., 2004), but that of R6/1 fibers, a different HD mouse model, was not
488 significantly different from control (Rozas et al., 2011). Our use of relatively blunt electrodes was
489 required for voltage clamp experiments but prevented reliable estimates of the resting
490 membrane potential. Thus, as we have done previously (Novak et al., 2015), we used single
491 sharp electrodes that minimize membrane damage to record the resting membrane potential of
492 extensor digitorum longus fibers from control (1 male and 2 female mice, 31 fibers) and R6/2 (1
493 male and 2 female mice, 30 fibers) mice. The resting membrane potential of R6/2 (-76.6 ± 0.7
494 mV) was significantly depolarized compared to control (-82.4 ± 0.5 mV) fibers ($p = 0.007$, t-test
495 where $t = -5.078$ with 4 df).

496 **Neuromuscular transmission under voltage and current clamp**

497 Our data showing depressed neuromuscular transmission in HD differs from other
498 studies that used current clamp recordings (Romero et al., 2008; Rozas et al., 2011). The
499 previous studies were completed prior to our reports describing the reduced membrane
500 conductances and capacitance in HD skeletal muscle (Waters et al., 2013; Miranda et al.,
501 2017). Given our work on the hyperexcitability of R6/2 fibers, we hypothesized that current
502 clamping the endplate in HD would yield different and potentially misleading results compared to
503 voltage clamp. To test this, we measured miniature endplate potentials (mEPPs) and evoked
504 endplate potentials (eEPPs) from a subset of R6/2 (3 male and 3 female mice, 64 fibers) and
505 control NMJs (2 male and 2 female mice, 36 fibers) that we also used to obtain voltage clamp
506 measurements. The mEPPs and eEPPs were normalized ($mEPP_{norm}$ and $eEPP_{norm}$) for changes
507 in the resting membrane potential and the evoked potentials were further corrected for nonlinear
508 summation ($eEPP_{corr}$) by replicating the method used for studying the NMJ in R6/1 mice (Rozas
509 et al., 2011). We found that the $mEPP_{norm}$ from R6/2 fibers (1.29 ± 0.07 mV) tended to be larger
510 than in control fibers (1.08 ± 0.04 mV), but did not quite reach our cut off for statistical
511 significance (Fig. 8A, $p=0.071$, t-test where $t=-2.08$ with 8 df). The R6/2 $eEPP_{corr}$ (58.1 ± 3.2
512 mV) were not significantly different from control (54.7 ± 1.4 mV) (Fig. 8B; $p=0.45$, t-test where
513 $t=-0.08$ with 8 df). These results were in stark contrast to the voltage clamp measurements
514 obtained from the same fibers, in which the average R6/2 mEPC charge and eEPC charge were
515 significantly smaller compared to control (Fig. 8A,B). Estimates of quantal content tended to be
516 lower from current clamp recordings (QC_{IC}) than voltage clamp (QC), which is consistent with
517 previous work that examined neuromuscular transmission under both conditions (Wood and
518 Slater, 1997). It happened that the estimates of QC were lower in R6/2 fibers compared to
519 control in both the current and voltage clamp recordings. However, QC estimates of control and
520 R6/2 NMJs under current clamp were lower than the QC obtained under voltage clamp. These

521 results indicate that the nonlinearity corrections (McLachlan and Martin, 1981) commonly used
522 in current clamp studies of synaptic transmission are not easily applicable to disease models
523 with disrupted postsynaptic membrane properties.

524

525 **Estimates of p_{rel} and n**

526 To determine whether the decrease in QC was due to a reduction in the probability of vesicle
527 release (p_{rel}) or the number of functional vesicle release sites (n), we used a previously
528 described graphical method based on binomial statistics (Clements and Silver, 2000; Wang et
529 al., 2010) to estimate p_{rel} and n with data collected in physiological Ca^{2+} and Mg^{2+} (Fig. 9). To
530 minimize the contribution of depression in the R6/2 NMJs, we determined p_{rel} and n from evoked
531 potentials 5 – 24 elicited at 0.5 Hz (Fig. 6). Briefly, we plotted experimental values of QC and
532 $\text{Var}(\text{QC})$ on two superimposed models of QC and $\text{Var}(\text{QC})$. One model shows QC and $\text{Var}(\text{QC})$
533 if p_{rel} was varied and n was held constant (parabolas). In this model, $\text{Var}(\text{QC}) = 0$ if no vesicles
534 are released ($p_{\text{rel}} = 0$) or if vesicles are released from all available sites ($p_{\text{rel}} = 1$); the maximum
535 $\text{Var}(\text{QC})$ occurs when $p_{\text{rel}} = 0.5$. For reference, we show parabolas for $n = 5, 10, 20, 40, 60,$ and
536 80 . We estimated n using experimental QC and $\text{Var}(\text{QC})$ values and equation (5) in the
537 Methods. The intersecting straight lines of the other model show QC and $\text{Var}(\text{QC})$ if n was
538 varied and p_{rel} was constant. We determined p_{rel} using experimental QC values and estimates of
539 n using the relationship of $QC = np$. As shown in Figure 9, the estimated n for R6/2 NMJs (52.3
540 ± 3.0 release sites) was trending lower than control (58.9 ± 2.6 release sites, $p=0.12$, t-test
541 where $t=1.662$ with 15 df). Estimates of p_{rel} were similar for R6/2 (0.81 ± 0.03) and control (0.84
542 ± 0.01) NMJs ($p=0.31$, Mann-Whitney rank sum test, where $U=24$). These results suggest that
543 reductions in n contribute more to the lower R6/2 QC than reductions in p .

544

545 **Neuromuscular morphology**

546 A reduction in n could arise from alterations in NMJ morphology. For example, a loss of
547 active sites could be caused by atrophy of R6/2 NMJs, which has been shown to occur in
548 proportion to the muscle atrophy (Ribchester et al., 2004). We examined NMJ morphology in
549 whole mount LAL preparations from 1 male and 4 female late-stage R6/2 mice (63 fibers) and 3
550 male and 3 female controls (70 fibers). Motor endplates were visualized based on the binding of
551 Alexa 555-conjugated α -bungarotoxin to nAChRs. Vesicle release sites were identified by
552 immunostaining of the protein bassoon, a widely used marker for active zones in the synapses
553 of central and peripheral tissues (Dieck et al., 1998; Nishimune et al., 2004; Spaulding et al.,
554 2016). Nearly every R6/2 NMJ and all control NMJs examined had a normal “pretzel-like”
555 morphology with bassoon punctae in apposition to nAChRs and no obvious fragmentation (Fig.
556 10A,B). One exception was an R6/2 NMJ with clear bassoon immunoreactivity that juxtaposed
557 an endplate with only partial coverage of nAChRs. Other studies have shown abnormalities in a
558 small fraction of HD NMJs (Ribchester et al., 2004; de Aragao et al., 2016). However, the
559 decrease in average R6/2 n would need to be explained by a consistent or uniform NMJ
560 change.

561 To quantitate NMJ morphology, the endplate area was determined by circumscribing the
562 semi-circular/elliptical nAChR staining region (Fig. 10A,B, left panels). The average R6/2
563 endplate area ($357 \pm 45 \mu\text{m}^2$) trended 23% smaller than that of control ($463 \pm 37 \mu\text{m}^2$) (Fig. 10C;
564 $p=0.10$, t-test where $t=1.82$ with 9 df). Additionally, the fraction of the endplate occupied by
565 nAChR (% synaptic area) was significantly less in R6/2 ($50.9 \pm 3.9\%$) than control ($63.2 \pm 1.4\%$)
566 fibers (Fig 10D, $p=0.01$, t-test where $t=3.20$ with 9 df). These percentages correspond to a
567 38% reduction in actual synaptic area of R6/2 endplates ($182 \mu\text{m}^2$) compared to control
568 ($293 \mu\text{m}^2$). To assess the relationship between bassoon and nAChRs, we estimated the
569 overlap coefficient, an intensity independent parameter that was 1.0 if every green pixel
570 (bassoon) colocalized with a red pixel (nAChR). The overlap coefficients of R6/2 (0.98 ± 0.01)

571 and control (0.99 ± 0.01) NMJs were not significantly different (Fig. 10E; $p=0.66$, Mann-Whitney
572 rank sum test with $U=12$). Also, the colocalization coefficient, which indicates the contribution of
573 bassoon to the colocalized regions, was not significantly different in R6/2 (0.39 ± 0.13)
574 compared to control (0.42 ± 0.12) NMJs ($p=0.86$, Mann-Whitney rank sum test with $U=12$). In
575 summary, bassoon tightly colocalized with nAChR in control and R6/2 NMJs and the decrease
576 in vesicle release sites suggested by the binomial statistics appears to be explained by a
577 reduction in the synaptic area of R6/2 NMJs.

578

579 **High frequency stimulation**

580 Normal muscle function requires that motor neurons release vesicles during trains of
581 stimulation. To assess the ability of R6/2 NMJs to maintain higher frequency trains of activity,
582 we stimulated the motor nerve with 10 trains at 10 s intervals. Each train consisted of 10
583 stimulations in 200 ms (50 Hz). We measured the trains in physiological Ca^{2+} and Mg^{2+} in the
584 same fibers we used to assess muscle hyperexcitability and QC. Figure 11 shows eEPCs
585 recorded during single trains in control (Fig. 11A) and R6/2 (Fig. 11B) fibers. To assess the
586 modulation of neuromuscular transmission during activity, we divided each eEPC amplitude by
587 the maximum eEPC in a train to obtain a normalized eEPC amplitude (Fig. 11C). During high
588 frequency trains, the overall degree of depression (last eEPC / first eEPC in a train) was
589 significantly greater in R6/2 NMJs (0.71 ± 0.02) compared to control (0.83 ± 0.01 , $p=2.6 \times 10^{-4}$,
590 t-test where $t=4.74$ with 14 df); note, a lower value is indicative of greater depression.

591 **DISCUSSION**592 **R6/2 muscle innervation**

593 Previous work reported that atrophied R6/2 skeletal muscle had an increased sensitivity
594 to acetylcholine and anode-break action potentials, which are characteristics of denervation
595 (Ribchester et al., 2004). They described the phenotype as “denervation-like” because they
596 found no evidence of physical denervation and observed minor morphological changes in only a
597 small fraction of R6/2 NMJs. Nonetheless, a more recent study reported motor unit loss and
598 denervation in R6/2 muscle based on changes in twitch tension in response to stimuli of
599 increasing strength (Mielcarek et al., 2015). It was further proposed in the same study that the
600 hyperexcitability in R6/2 skeletal muscle was the result of denervation. Considering that
601 denervation is known to cause skeletal muscle atrophy and hyperexcitability (Albuquerque and
602 McIsaac, 1970; Thesleff and Ward, 1975), it was important to further examine whether
603 denervation occurs in HD.

604 We found that all of the postsynaptic sites were adjoined to presynaptic terminals in R6/2
605 muscle, tight bassoon and nAChR colocalization, and that the expression level of nAChR γ , SK3,
606 and Scn5a, all of which upregulate upon denervation, were normal or downregulated in R6/2
607 muscle. Also, if R6/2 muscle were denervated, we would expect to find a mixed population of
608 fibers with distinct excitability and NMJ characteristics, as is seen in other motor neuron
609 diseases that display denervation/reinnervation patterns, such as ALS (Rocha et al., 2013).
610 However, we found that the hyperexcitability of the fibers and the characteristics of
611 neuromuscular transmission were normally distributed.

612 Perhaps the examination of R6/2 motor unit number (Mielcarek et al., 2015) was
613 influenced by motor neuron hyperexcitability; their method of quantifying motor units assumes
614 that motor nerve excitability is the same in disease and control muscle. Supporting this
615 possibility, hyperexcitability or decreased potassium currents have been reported in medium

616 spiny neurons and astrocytes in mouse models of HD (Ariano et al., 2005; Rocha et al., 2013;
617 Tong et al., 2014).

618 This study and the results in Ribchester, *et al.* show that denervation is not occurring or
619 only develops in an extremely small number of R6/2 muscle fibers. The “denervation-like”
620 effects found in R6/2 muscle (Ribchester et al., 2004) likely arise from decreases in the resting
621 chloride and potassium currents that coincide with aberrant mRNA processing (Waters et al.,
622 2013; Miranda et al., 2017).

623

624 **Voltage clamp analysis of neuromuscular transmission**

625 Because the muscle membrane potential does not change during our voltage clamp
626 recordings, mEPCs and eEPCs are independent of the muscle membrane properties. Previous
627 studies of HD neuromuscular transmission, mostly completed before we showed the disrupted
628 R6/2 muscle membrane properties, used current clamp recordings (Ribchester et al., 2004;
629 Romero et al., 2008; Rozas et al., 2011; de Aragao et al., 2016). One study corrected for
630 nonlinearities using methods that assume the postsynaptic membrane properties are unaltered,
631 including a correction factor for membrane capacitance (Rozas et al., 2011). To assess the
632 effect of the altered R6/2 muscle membrane conductances and capacitance (Waters et al.,
633 2013; Miranda et al., 2017) on the corrected data, we measured neuromuscular transmission in
634 the same fibers under current and voltage clamp. In voltage clamp, the spontaneous and
635 evoked responses in R6/2 fibers were decreased relative to control; whereas under current
636 clamp, they were larger. Thus, because of the altered muscle membrane properties, reduced
637 synaptic transmission may actually appear enhanced in current clamp records. These results
638 highlight the need to account for the postsynaptic membrane properties in synaptic studies and,
639 if possible, record the endplate currents in voltage clamp. Such voltage clamp studies may be
640 exceedingly difficult or impossible with central synapses, but can be achieved in large
641 monosynaptic muscle fibers.

642

643 **Neuromuscular transmission in HD**

644 Under conditions of low Ca^{2+} and high Mg^{2+} , we found no clear impairments in R6/2
645 neuromuscular transmission. If anything, the trend was for larger R6/2 eEPCs and QC
646 compared to control in the low Ca^{2+} conditions. Thus, under conditions in which vesicle release
647 and the need for vesicle mobilization are minimized, synaptic transmission in R6/2 muscle is
648 normal.

649 However, in normal extracellular Ca^{2+} and Mg^{2+} , the mEPC and eEPC charge are
650 reduced in R6/2 compared to controls NMJs. Additionally, the mEPCs and eEPCs are
651 prolonged in R6/2 fibers. A decrease in acetylcholinesterase function would explain the
652 prolonged mEPC and eEPC kinetics but is contradicted by the decrease in mEPC and eEPC
653 charge. A change in the nAChR isoform seems unlikely since we found no change in the
654 expression level of nAChR γ . Moreover, a previous study found no change in the density of
655 nAChRs in R6/2 NMJs (Ribchester et al., 2004). Possible explanations for the mEPC and eEPC
656 properties are impaired vesicle fusion and posttranslational modification of nAChRs.

657 Our analysis of eEPC variance suggests a reduction in the number of R6/2 vesicle
658 release sites (n), which we found coincides with a decrease in the synaptic area of R6/2 NMJ.
659 At first pass, a decrease in the physical number of active sites may not seem compatible with
660 our observed dependence of QC on Ca^{2+} (normal QC in low but reduced in normal Ca^{2+}).
661 However, recent reports show that n is dependent on Ca^{2+} (Wang et al., 2010), indicating that n
662 also depends on physiological factors such as vesicle mobilization.

663 Our data showing depression in neuromuscular transmission under trains of stimulation,
664 even at 0.5 Hz stimulation, indicate impaired vesicle mobilization in HD. Other neuromuscular
665 studies using FM styryl dyes have produced conflicting results, with no changes in vesicle
666 recycling reported in R6/1 mice (Rozas et al., 2011) and depressed vesicle exocytosis reported
667 for BACHD mice (de Aragao et al., 2016). Supporting defects in vesicle mobilization, the

668 huntingtin protein is thought to interact with clathrin-coated vesicles and proteins involved in
669 vesicle trafficking (Velier et al., 1998). Furthermore, a study on CNS synapses in HD found that
670 R6/2 mice demonstrated a progressive loss of complexin II, a known SNARE complex-binding
671 protein believed to be involved in exocytosis modulation and vesicle release synchronization
672 (Morton and Edwardson, 2001; Morton et al., 2001; Freeman and Morton, 2004; Lin et al.,
673 2013). Thus, a decrease in complexin activity could result in an apparent decrease in functional
674 active sites as vesicle fusion is stimulated.

675 The neuromuscular depression in late-stage HD muscle likely depends on disease
676 progression and may compensate for the muscle hyperexcitability. Similarly, the depolarized
677 resting membrane potential may further counter the muscle hyperexcitability. Previous studies
678 using the R6/1 mouse and drosophila models of HD at an earlier stage of the disease show
679 increased neuromuscular transmission (Romero et al., 2008; Rozas et al., 2011). These results
680 cannot be fully explained by their use of current clamp instead of voltage clamp. For example,
681 we found a significantly lower mEPC frequency in late-stage R6/2 muscle, which is consistent
682 with a previous current clamp study (Ribchester et al., 2004) and is independent of using
683 voltage or current clamp. In comparison, the frequency of mEPPs was not significantly different
684 in early-stage HD muscle from R6/1, R6/2, and BACHD mice as well as drosophila (Ribchester
685 et al., 2004; Romero et al., 2008; Rozas et al., 2011; de Aragao et al., 2016). A time course
686 study of the NMJ, with voltage clamp recordings, will be necessary to determine if HD
687 neuromuscular transmission transitions from elevated to depressed during disease progression.
688 Such studies can help us determine if the depressed neuromuscular transmission we observed
689 in late-stage R6/2 compensates for the muscle hyperexcitability. This would be supported by
690 NMJ depression beginning after the onset of the muscle membrane defects, which we have
691 shown begins at or before 5 weeks of age in R6/2 mice (Miranda et al., 2017). Similarly,
692 enhanced neuromuscular transmission in young R6/2 muscle, as observed in drosophila larva
693 (Romero et al., 2008), would support nerve-to-muscle effects.

694 It has become increasingly accepted that HD is a multi-system disorder. Defects in both
695 the brain and skeletal muscle likely contribute to the motor symptoms, perhaps in a vicious
696 cycle. Adding to this, the defects we found in neuromuscular transmission could arise from
697 mutant *huntingtin* expression in motor neurons. The NMJ is an excellent model to examine the
698 interplay between neuronal and muscle defects in HD. Furthermore, our use of voltage clamp to
699 measure neuromuscular transmission provides the most detailed analysis of synaptic
700 transmission in HD to date and can serve as a model for the less accessible multi-synaptic
701 networks of the central nervous system. Clinically, the striking depression we observed in R6/2
702 neurotransmission, even at 0.5 Hz stimulation, could help explain the motor impersistence
703 experienced by many HD patients (Gordon et al., 2000; Reilmann et al., 2001). Time course
704 studies, although resource-intensive, could help reveal an underlying primary defect in the
705 muscle, motor neuron, or central nervous system that drives secondary defects in the other
706 systems. Perhaps more likely, the widespread expression of mutant huntingtin causes
707 independent and subsequently interacting defects in multiple tissues. Regardless, therapies that
708 enhance neuromuscular transmission or reduce muscle hyperexcitability represent a largely
709 unconsidered class of agents that may lessen the motor symptoms in late-stage HD patients.
710

711 REFERENCES

712

- 713 Adams L, Carlson BM, Henderson L, Goldman D (1995) Adaptation of nicotinic acetylcholine
714 receptor, myogenin, and MRF4 gene expression to long-term muscle denervation. *J Cell*
715 *Biol* 131:1341-1349.
- 716 Albuquerque EX, Mclsaac RJ (1970) Fast and slow mammalian muscles after denervation.
717 *Experimental Neurology* 26:183-202.
- 718 Ariano MA, Cepeda C, Calvert CR, Flores-Hernandez J, Hernandez-Echeagaray E, Klapstein GJ,
719 Chandler SH, Aronin N, DiFiglia M, Levine MS (2005) Striatal potassium channel
720 dysfunction in Huntington's disease transgenic mice. *J Neurophysiol* 93:2565-2574.
- 721 Bhide PG, Day M, Sapp E, Schwarz C, Sheth A, Kim J, Young AB, Penney J, Golden J, Aronin N,
722 DiFiglia M (1996) Expression of normal and mutant huntingtin in the developing brain. *J*
723 *Neurosci* 16:5523-5535.
- 724 Busse ME, Hughes G, Wiles CM, Rosser AE (2008) Use of hand-held dynamometry in the
725 evaluation of lower limb muscle strength in people with Huntington's disease. *Journal of*
726 *Neurology* 255:1534-1540.
- 727 Clements JD, Silver RA (2000) Unveiling synaptic plasticity: a new graphical and analytical
728 approach. *Trends in neurosciences* 23:105-113.
- 729 de Aragao BC, Rodrigues HA, Valadao PA, Camargo W, Naves LA, Ribeiro FM, Guatimosim C
730 (2016) Changes in structure and function of diaphragm neuromuscular junctions from
731 BACHD mouse model for Huntington's disease. *Neurochem Int*.
- 732 Dieck S, Sanmartí-Vila L, Langnaese K, Richter K, Kindler S, Soyke A, Wex H, Smalla K-H, Kämpf
733 U, Fränzer J-T, Stumm M, Garner CC, Gundelfinger ED (1998) Bassoon, a Novel Zinc-
734 finger CAG/Glutamine-repeat Protein Selectively Localized at the Active Zone of
735 Presynaptic Nerve Terminals. *The Journal of Cell Biology* 142:499-509.
- 736 Ehrnhoefer DE, Skotte NH, Ladha S, Nguyen Y, Qiu X, Deng Y, Huynh KT, Engemann S, Nielsen
737 SM, Becanovic K, Leavitt BR, Hasholt L, Hayden MR (2014) p53 increases caspase-6
738 expression and activation in muscle tissue expressing mutant huntingtin. *Human*
739 *Molecular Genetics* 23:717-729.
- 740 Favero M, Jiang DJ, Chiamulera C, Cangiano A, Fumagalli GF (2008) Expression of small-
741 conductance calcium-activated potassium channels (SK3) in skeletal muscle: regulation
742 by muscle activity. *J Physiol* 586:4763-4774.
- 743 Freeman W, Morton AJ (2004) Regional and progressive changes in brain expression of
744 complexin II in a mouse transgenic for the Huntington's disease mutation. *Brain*
745 *research bulletin* 63:45-55.
- 746 Gordon AM, Quinn L, Reilmann R, Marder K (2000) Coordination of prehensile forces during
747 precision grip in Huntington's disease. *Exp Neurol* 163:136-148.
- 748 Group THsDCR (1993) A novel gene containing a trinucleotide repeat that is expanded and
749 unstable on Huntington's disease chromosomes. *J Cell* 72:971-983.
- 750 Gu Y, Hall ZW (1988a) Characterization of acetylcholine receptor subunits in developing and in
751 denervated mammalian muscle. *J Biol Chem* 263:12878-12885.

- 752 Gu Y, Hall ZW (1988b) Immunological evidence for a change in subunits of the acetylcholine
753 receptor in developing and denervated rat muscle. *Neuron* 1:117-125.
- 754 Hartzell HC, Fambrough DM (1972) Acetylcholine receptors. Distribution and extrajunctional
755 density in rat diaphragm after denervation correlated with acetylcholine sensitivity. *J*
756 *Gen Physiol* 60:248-262.
- 757 Hering T, Braubach P, Landwehrmeyer GB, Lindenberg KS, Melzer W (2016) Fast-to-Slow
758 Transition of Skeletal Muscle Contractile Function and Corresponding Changes in Myosin
759 Heavy and Light Chain Formation in the R6/2 Mouse Model of Huntington's Disease.
760 *PLoS One* 11:e0166106.
- 761 Hutter OF, Noble D (1960) The chloride conductance of frog skeletal muscle. *J Physiol* 151:89-
762 102.
- 763 Jacobson D, Herson PS, Neelands TR, Maylie J, Adelman JP (2002) SK channels are necessary but
764 not sufficient for denervation-induced hyperexcitability. *Muscle Nerve* 26:817-822.
- 765 Kosinski CM, Schlangen C, Gellerich FN, Gizatullina Z, Deschauer M, Schiefer J, Young AB,
766 Landwehrmeyer G, Toyka KV, Sellhaus B, Lindenberg KS (2007) Myopathy as a first
767 symptom of Huntington's disease in a Marathon runner. *Movement Disorders* 22:1637-
768 1640.
- 769 Kues WA, Brenner HR, Sakmann B, Witzemann V (1995) Local neurotrophic repression of gene
770 transcripts encoding fetal AChRs at rat neuromuscular synapses. *J Cell Biol* 130:949-957.
- 771 Lin MY, Rohan JG, Cai H, Reim K, Ko CP, Chow RH (2013) Complexin facilitates exocytosis and
772 synchronizes vesicle release in two secretory model systems. *J Physiol* 591:2463-2473.
- 773 Liu L, Xie F, Wei K, Hao XC, Li P, Cao J, Min S (2016) Sepsis induced denervation-like changes at
774 the neuromuscular junction. *J Surg Res* 200:523-532.
- 775 Lo DC, Hughes RE (2010) *Neurobiology of Huntington's disease: applications to drug discovery.*
776 Boca Raton: CRC Press/Taylor & Francis Group.
- 777 Lodi R, Schapira AH, Manners D, Styles P, Wood NW, Taylor DJ, Warner TT (2000) Abnormal in
778 vivo skeletal muscle energy metabolism in Huntington's disease and
779 dentatorubropallidoluysian atrophy. *Annals of neurology* 48:72-76.
- 780 Lomo T, Rosenthal J (1972) Control of ACh sensitivity by muscle activity in the rat. *J Physiol*
781 221:493-513.
- 782 Lomo T, Westgaard RH (1975) Further studies on the control of ACh sensitivity by muscle
783 activity in the rat. *J Physiol* 252:603-626.
- 784 Lupa MT, Krzemien DM, Schaller KL, Caldwell JH (1995) Expression and distribution of sodium
785 channels in short- and long-term denervated rodent skeletal muscles. *J Physiol* 483 (Pt
786 1):109-118.
- 787 Luthi-Carter R, Hanson SA, Strand AD, Bergstrom DA, Chun W, Peters NL, Woods AM, Chan EY,
788 Kooperberg C, Krainc D, Young AB, Tapscott SJ, Olson JM (2002) Dysregulation of gene
789 expression in the R6/2 model of polyglutamine disease: parallel changes in muscle and
790 brain. *Human Molecular Genetics* 11:1911-1926.
- 791 Magrassi L, Purves D, Lichtman JW (1987) Fluorescent probes that stain living nerve terminals. *J*
792 *Neurosci* 7:1207-1214.
- 793 McLachlan EM, Martin AR (1981) Non linear summation of end plate potentials in the frog and
794 mouse. *The Journal of Physiology* 311:307-324.

- 795 Mielcarek M, Toczek M, Smeets CJ, Franklin SA, Bondulich MK, Jolinon N, Muller T, Ahmed M,
796 Dick JR, Piotrowska I, Greensmith L, Smolenski RT, Bates GP (2015) HDAC4-myogenin
797 axis as an important marker of HD-related skeletal muscle atrophy. *PLoS Genet*
798 11:e1005021.
- 799 Miranda DR, Wong M, Romer SH, McKee C, Garza-Vasquez G, Medina AC, Bahn V, Steele AD,
800 Talmadge RJ, Voss AA (2017) Progressive Cl⁻ channel defects reveal disrupted skeletal
801 muscle maturation in R6/2 Huntington's mice. *J Gen Physiol* 149:55-74.
- 802 Morton AJ, Edwardson JM (2001) Progressive depletion of complexin II in a transgenic mouse
803 model of Huntington's disease. *Journal of neurochemistry* 76:166-172.
- 804 Morton AJ, Faull RL, Edwardson JM (2001) Abnormalities in the synaptic vesicle fusion
805 machinery in Huntington's disease. *Brain research bulletin* 56:111-117.
- 806 Moss SJ, Beeson DM, Jackson JF, Darlison MG, Barnard EA (1987) Differential expression of
807 nicotinic acetylcholine receptor genes in innervated and denervated chicken muscle.
808 *EMBO J* 6:3917-3921.
- 809 Neelands TR, Herson PS, Jacobson D, Adelman JP, Maylie J (2001) Small-conductance calcium-
810 activated potassium currents in mouse hyperexcitable denervated skeletal muscle. *J*
811 *Physiol* 536:397-407.
- 812 Nishimune H, Sanes JR, Carlson SS (2004) A synaptic laminin-calcium channel interaction
813 organizes active zones in motor nerve terminals. *Nature* 432:580-587.
- 814 Novak KR, Norman J, Mitchell JR, Pinter MJ, Rich MM (2015) Sodium channel slow inactivation
815 as a therapeutic target for myotonia congenita. *Ann Neurol* 77:320-332.
- 816 Pribnow D, Johnson-Pais T, Bond CT, Keen J, Johnson RA, Janowsky A, Silvia C, Thayer M, Maylie
817 J, Adelman JP (1999) Skeletal muscle and small-conductance calcium-activated
818 potassium channels. *Muscle Nerve* 22:742-750.
- 819 Reilmann R, Kirsten F, Quinn L, Henningsen H, Marder K, Gordon AM (2001) Objective
820 assessment of progression in Huntington's disease: a 3-year follow-up study. *Neurology*
821 57:920-924.
- 822 Ribchester RR, Thomson D, Wood NI, Hinks T, Gillingwater TH, Wishart TM, Court FA, Morton AJ
823 (2004) Progressive abnormalities in skeletal muscle and neuromuscular junctions of
824 transgenic mice expressing the Huntington's disease mutation. *Eur J Neurosci* 20:3092-
825 3114.
- 826 Rich MM, Kraner SD, Barchi RL (1999) Altered gene expression in steroid-treated denervated
827 muscle. *Neurobiol Dis* 6:515-522.
- 828 Rocha MC, Pousinha PA, Correia AM, Sebastiao AM, Ribeiro JA (2013) Early changes of
829 neuromuscular transmission in the SOD1(G93A) mice model of ALS start long before
830 motor symptoms onset. *PLoS One* 8:e73846.
- 831 Rogart RB, Cribbs LL, Muglia LK, Kephart DD, Kaiser MW (1989) Molecular cloning of a putative
832 tetrodotoxin-resistant rat heart Na⁺ channel isoform. *Proc Natl Acad Sci U S A* 86:8170-
833 8174.
- 834 Romero E, Cha G-H, Verstreken P, Ly CV, Hughes RE, Bellen HJ, Botas J (2008) Suppression of
835 Neurodegeneration and Increased Neurotransmission Caused by Expanded Full-Length
836 Huntingtin Accumulating in the Cytoplasm. *Neuron* 57:27-40.

- 837 Rozas JL, Gomez-Sanchez L, Tomas-Zapico C, Lucas JJ, Fernandez-Chacon R (2011) Increased
838 neurotransmitter release at the neuromuscular junction in a mouse model of
839 polyglutamine disease. *J Neurosci* 31:1106-1113.
- 840 Sekiguchi K, Kanda F, Mitsui S, Kohara N, Chihara K (2012) Fibrillation potentials of denervated
841 rat skeletal muscle are associated with expression of cardiac-type voltage-gated sodium
842 channel isoform Nav1.5. *Clin Neurophysiol* 123:1650-1655.
- 843 She P, Zhang Z, Marchionini D, Diaz WC, Jetton TJ, Kimball SR, Vary TC, Lang CH, Lynch CJ (2011)
844 Molecular characterization of skeletal muscle atrophy in the R6/2 mouse model of
845 Huntington's disease. *Am J Physiol Endocrinol Metab* 301:E49-61.
- 846 Spaulding EL, Sleigh JN, Morelli KH, Pinter MJ, Burgess RW, Seburn KL (2016) Synaptic Deficits at
847 Neuromuscular Junctions in Two Mouse Models of Charcot-Marie-Tooth Type 2d.
848 *Journal of Neuroscience* 36:3254-3267.
- 849 Steinmeyer K, Ortland C, Jentsch TJ (1991a) Primary structure and functional expression of a
850 developmentally regulated skeletal muscle chloride channel. *Nature* 354:301-304.
- 851 Steinmeyer K, Klocke R, Ortland C, Gronemeier M, Jockusch H, Grunder S, Jentsch TJ (1991b)
852 Inactivation of muscle chloride channel by transposon insertion in myotonic mice.
853 *Nature* 354:304-308.
- 854 Strand AD, Aragaki AK, Shaw D, Bird T, Holton J, Turner C, Tapscott SJ, Tabrizi SJ, Schapira AH,
855 Kooperberg C, Olson JM (2005) Gene expression in Huntington's disease skeletal muscle:
856 a potential biomarker. *Hum Mol Genet* 14:1863-1876.
- 857 Thesleff S, Ward MR (1975) Studies on the mechanism of fibrillation potentials in denervated
858 muscle. *J Physiol* 244:313-323.
- 859 Tong X, Ao Y, Faas GC, Nwaobi SE, Xu J, Haustein MD, Anderson MA, Mody I, Olsen ML,
860 Sofroniew MV, Khakh BS (2014) Astrocyte Kir4.1 ion channel deficits contribute to
861 neuronal dysfunction in Huntington's disease model mice. *Nat Neurosci* 17:694-703.
- 862 Turner C, Cooper MJ, Schapira AHV (2007) Clinical correlates of mitochondrial function in
863 Huntington's disease muscle. *Movement Disorders* 22:1715-1721.
- 864 Valadao PA, de Aragao BC, Andrade JN, Magalhaes-Gomes MP, Foureaux G, Joviano-Santos JV,
865 Nogueira JC, Ribeiro FM, Tapia JC, Guatimosim C (2017) Muscle atrophy is associated
866 with cervical spinal motoneuron loss in BACHD mouse model for Huntington's disease.
867 *Eur J Neurosci* 45:785-796.
- 868 Velier J, Kim M, Schwarz C, Kim TW, Sapp E, Chase K, Aronin N, DiFiglia M (1998) Wild-type and
869 mutant huntingtins function in vesicle trafficking in the secretory and endocytic
870 pathways. *Exp Neurol* 152:34-40.
- 871 Voss AA (2009) Extracellular ATP inhibits chloride channels in mature mammalian skeletal
872 muscle by activating P2Y(1) receptors. *J Physiol-London* 587:5739-5752.
- 873 Wang X, Pinter MJ, Rich MM (2010) Ca²⁺ Dependence of the Binomial Parameters p and n at
874 the Mouse Neuromuscular Junction. *Journal of Neurophysiology*.
- 875 Waters CW, Varuzhanyan G, Talmadge RJ, Voss AA (2013) Huntington disease skeletal muscle is
876 hyperexcitable owing to chloride and potassium channel dysfunction. *P Natl Acad Sci*
877 *USA* 110:9160-9165.
- 878 Wells RD, Ashizawa T (2006) Genetic instabilities and neurological diseases, 2nd Edition.
879 Amsterdam; Boston: Elsevier.

- 880 Witzemann V, Barg B, Nishikawa Y, Sakmann B, Numa S (1987) Differential regulation of muscle
881 acetylcholine receptor gamma- and epsilon-subunit mRNAs. FEBS Lett 223:104-112.
882 Wood SJ, Slater CR (1997) The contribution of postsynaptic folds to the safety factor for
883 neuromuscular transmission in rat fast- and slow-twitch muscles. J Physiol 500 (Pt
884 1):165-176.
885 Yang JS, Sladky JT, Kallen RG, Barchi RL (1991) TTX-sensitive and TTX-insensitive sodium channel
886 mRNA transcripts are independently regulated in adult skeletal muscle after
887 denervation. Neuron 7:421-427.
888

889 **Figure Legends**

890

891 **Figure 1.** Increased membrane time constant (τ_m) indicative of hyperexcitable R6/2 skeletal
892 muscle fibers. **A**, Injected current steps (top traces) and the resulting membrane potential
893 responses in representative control and R6/2 muscle fibers (bottom traces) in normal calcium.
894 **B**, Average control and R6/2 τ_m . **C**, Histogram of control (solid black bars) and R6/2 (striped
895 gray bars) τ_m . *Indicates a significant difference compared to control ($p=5.94 \times 10^{-6}$, t-test).
896 Regions of overlap as black striped bars. Error bars are \pm SEM.

897

898 **Figure 2.** Representative images of stained control and R6/2 neuromuscular junctions (NMJs)
899 from 12-week-old mice. Motor nerves and terminals were identified by a combination of
900 neurofilament staining (SMI-31) of axons and SV2b staining of synaptic vesicles (both in green;
901 Nerve). Motor endplates were labeled by staining of nicotinic acetylcholine receptors with
902 rhodamine-conjugated α -bungarotoxin (red; nAChRs). The regions of superimposed nerve and
903 nAChRs are yellow in the merged images. In both the control and R6/2 fibers, all nAChRs were
904 directly aligned with nerve terminals. Scale bar in lower right is 30 μ m.

905

906 **Figure 3.** Reverse transcriptase-polymerase chain reaction (RT-PCR) analyses of the
907 expression of denervation-induced gene mRNAs in R6/2 and control mice. **A**, Gel-based RT-
908 PCR for the expression of the nicotinic acetylcholine receptor γ -subunit (nAChR γ). Neither
909 control nor R6/2 tibialis anterior nor soleus muscles showed expression of nAChR γ . In contrast,
910 expression of nAChR γ was detectable in denervated (Dnv), but not control (Cont) mouse
911 gastrocnemius (Gast) muscle. Also, expression of nAChR γ was observed in postnatal day 1
912 (P1) hindlimb muscles (Hind) of mice. The M designates base-pair size markers. **B**, Real-time
913 RT-PCR analyses of nAChR γ , the small-conductance calcium-activated potassium channel

914 (SK3), and the cardiac muscle isoform of the voltage-gated sodium channel, Nav1.5 (Scn5a)
915 mRNAs relative to β 2-microglobulin in control and R6/2 mice. No significant changes in the
916 mRNAs for nAChR γ and SK3 were observed in R6/2 mouse tibialis anterior (left panel, nAChR γ :
917 $p=0.398$, t-test and SK3: $p=0.991$, t-test) and soleus (middle panel, nAChR γ : $p=0.289$, t-test and
918 SK3: $p=0.403$, t-test) muscle compared to control. There was a significant decrease in the levels
919 of Scn5a in R6/2 tibialis anterior ($p=0.025$, t-test) but not soleus muscle ($p=0.094$, t-test) relative
920 to control. In contrast, there was a marked increase in the expression of nAChR γ ($p=0.0099$, t-
921 test), SK3 ($p=0.0002$, t-test), and Scn5a ($p=0.0001$, t-test) mRNA in denervated gastrocnemius
922 relative to the innervated contralateral muscle in control mice ($n=4$ muscles/group). *Indicates a
923 significant difference. Error bars are \pm SEM.

924

925 **Figure 4.** The mEPC charge, eEPC charge, and quantal content (QC) in control and R6/2 NMJs
926 in low extracellular Ca $^{2+}$ (0.5 mM) and high Mg $^{2+}$ (4 mM). **A**, Superimposed representative eEPC
927 traces from control and R6/2 NMJs with an inset of superimposed representative mEPC traces
928 from the same NMJs under two-electrode voltage clamp. **B**, Histograms of average control
929 (solid black bars) and R6/2 (striped gray bars) mEPC charge, eEPC charge, and QC. Regions
930 of overlap as black striped bars.

931

932 **Figure 5.** The mEPC charge, eEPC charge, and quantal content (QC) in control and R6/2 NMJs
933 in physiological extracellular Ca $^{2+}$ (1.2 mM) and Mg $^{2+}$ (0.6 mM). **A and B**, Representative control
934 (**A**) and R6/2 (**B**) recordings under two-electrode voltage clamp showing mEPCs and eEPCs
935 (baseline adjusted to 0). **C and D**, Superimposed representative eEPC traces from control (**C**)
936 and R6/2 (**D**) NMJs with an inset of superimposed mEPC traces from the same NMJs. **E – G**,
937 Histograms of average control (solid black bars) and R6/2 (striped gray bars) mEPC charge (**E**),
938 eEPC charge (**F**), and quantal content (**G**). Regions of overlap as black striped bars.

939

940 **Figure 6.** Synaptic modulation at low frequency stimulation (0.5 Hz). **A**, Average control (10
 941 mice) and R6/2 (7 mice) eEPC charges normalized to the peak eEPC charge in a train of 60
 942 eEPCs stimulated at 0.5 Hz. **B**, Normalized eEPCs (postion 5 – 60 in train) from panel A
 943 showing the linear regression for control (solid black line) and R6/2 (solid gray line). Data are
 944 shown with the 95% confidence interval for each linear regression (control shaded black and
 945 R6/2 shaded gray). Error bars are \pm SEM.

946

947 **Figure 7.** Kinetics of control and R6/2 mEPCs and eEPCs. **A and B**, Average mEPC (**A**) and
 948 eEPC (**B**) from representative control (solid lines) and R6/2 (dashed lines) NMJs, each
 949 normalized to peak (peak value set to 1 for each endplate current). **C and D**, Histograms of the
 950 control (solid black bars) and R6/2 (striped gray bars) mEPC decay constants (**C**) and eEPC
 951 decay constants (**D**). Regions of overlap as black striped bars.

952

953 **Figure 8.** Comparison of NMJ transmission data collected under voltage clamp (mEPC and
 954 eEPC) and current clamp (mEPP_{norm} and eEPP_{corr}) from the same control (cntrl) and R6/2 fibers.
 955 **A**, mEPCs ($p=0.003$, t-test), but not mEPP_{norm} ($p=0.071$, t-test), were significantly lower in R6/2
 956 compared to control fibers. **B**, similarly, eEPCs ($p=6.4 \times 10^{-5}$, t-test), but not eEPP_{corr} ($p=0.45$, t-
 957 test), were significantly lower in R6/2 compared to control fibers. **C**, estimates of quantal content
 958 from voltage clamp (QC) and current clamp (QC_{IC}) were lower for R6/2 compared to control
 959 ($p=0.008$ and $p=0.02$, respectively, t-test). *Indicates a significant difference compared to control
 960 NMJs. Error bars are \pm SEM.

961

962 **Figure 9.** Var(QC) vs QC plot for estimating the probability of release (p_{rel}) and number of
 963 vesicle release sites (n). Experimental Var(QC) and QC data superimposed on two theoretical
 964 models (parabolas and straight lines). The parabolas model Var(QC) and QC while varying p_{rel}

965 and holding n constant. Straight lines model $\text{Var}(\text{QC})$ and QC while varying n and holding p_{rel}
966 constant. The lower QC (vesicle release per impulse) in R6/2 compared to control fibers was
967 primarily due to a lower n . Error bars are \pm SEM.

968

969 **Figure 10.** Comparison of R6/2 and control NMJs stained for postsynaptic nicotinic
970 acetylcholine receptors (nAChRs) and presynaptic bassoon proteins. **A and B**, representative
971 control (**A**) and R6/2 (**B**) NMJs stained for nAChRs on the motor endplate (red, left panel),
972 bassoon in the motor nerve terminals (green, middle panel), and the merge image of the nAChR
973 and bassoon staining (right panel). nAChRs were stained with α -bungarotoxin-Alexa 555 and
974 bassoon was detected by immunofluorescence. **C**, total endplate area for control (black bar)
975 and R6/2 (gray bar) NMJs determined by circumscribing the nAChR staining region. **D**, the
976 percent of the control (black bar) and R6/2 (gray bar) endplate occupied by nAChR. This
977 estimate of synaptic area was significantly less in R6/2 compared to control NMJs ($p=0.01$, t-
978 test). **E**, the overlap coefficient of bassoon to nAChR in control (black bar) and R6/2 (gray bar)
979 NMJs. A value of 1 indicates that each pixel of bassoon staining (green) colocalized with red
980 pixels (nAChR). *Indicates a significant difference compared to control NMJs. Error bars are \pm
981 SEM.

982

983 **Figure 11.** eEPC depression during high frequency (50 Hz) stimulation trains. **A and B**,
984 Representative raw traces for control (**A**) and R6/2 (**B**) NMJs. **C**, Average control (10 mice) and
985 R6/2 (7 mice) eEPC amplitudes normalized to the peak eEPC amplitude in a train of 10 eEPCs
986 at 50 Hz stimulation. Error bars are \pm SEM.

987

Figure 1

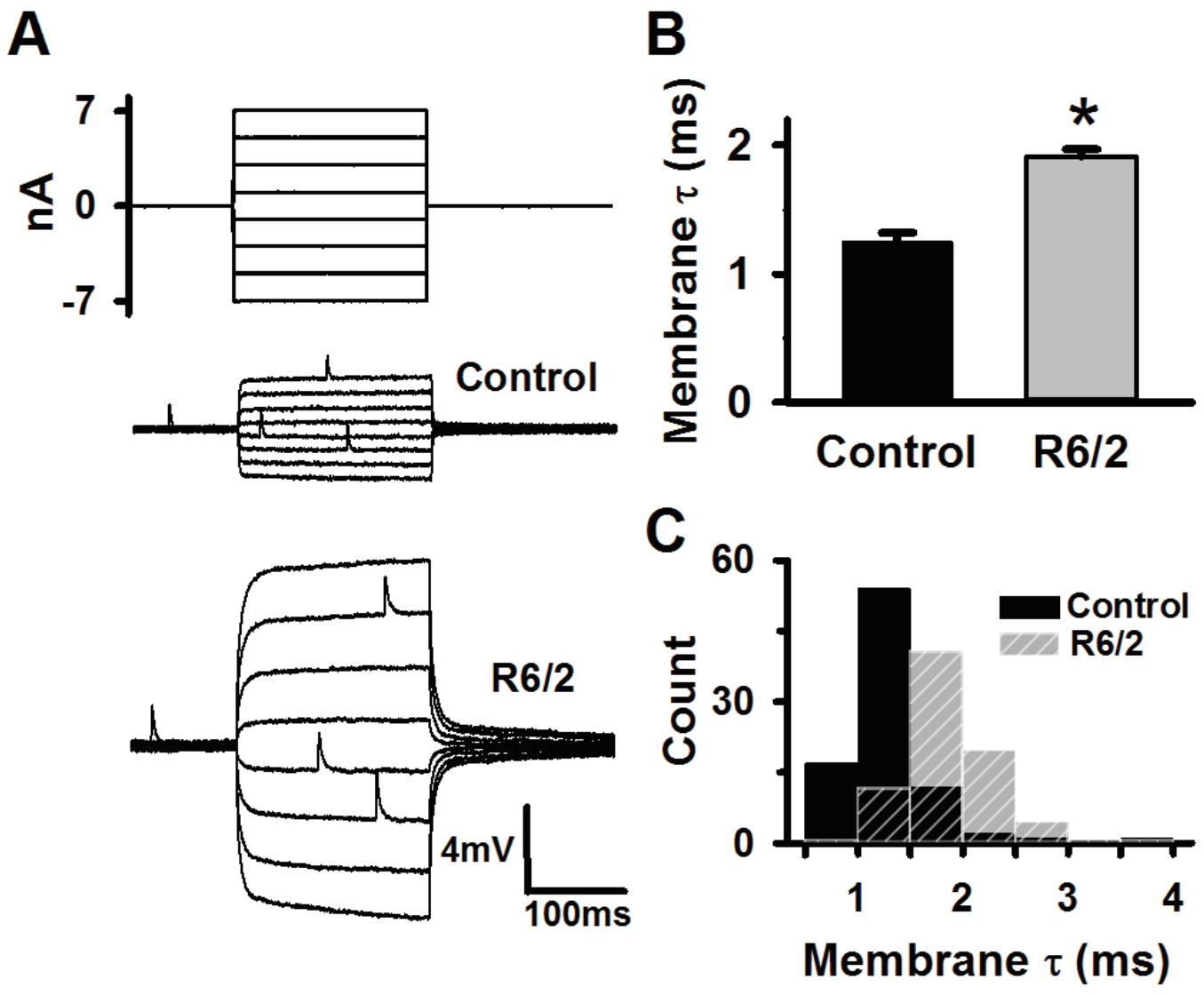


Figure 2

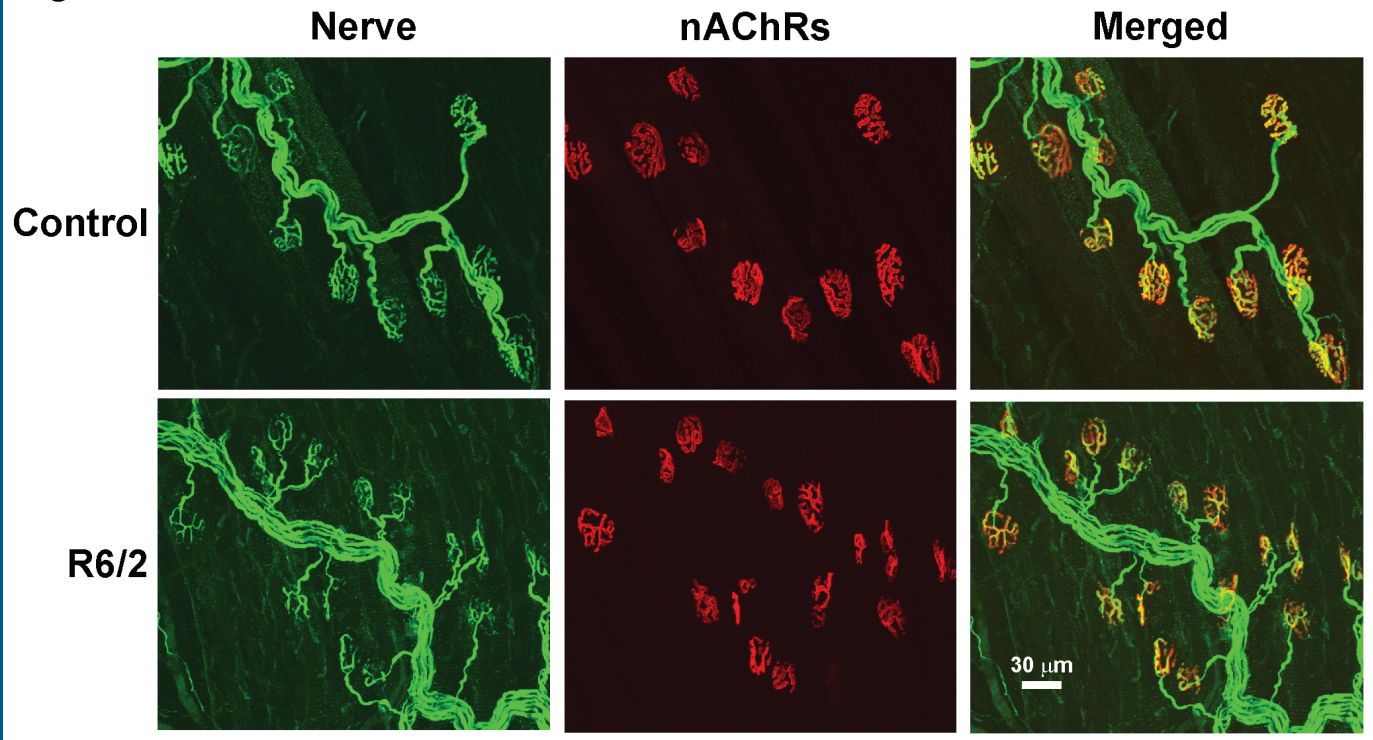


Figure 3

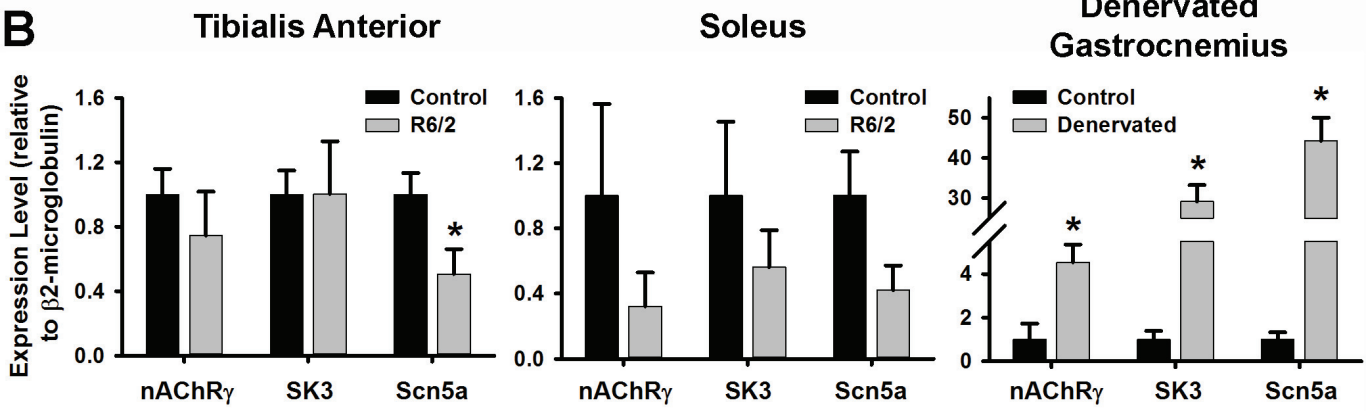
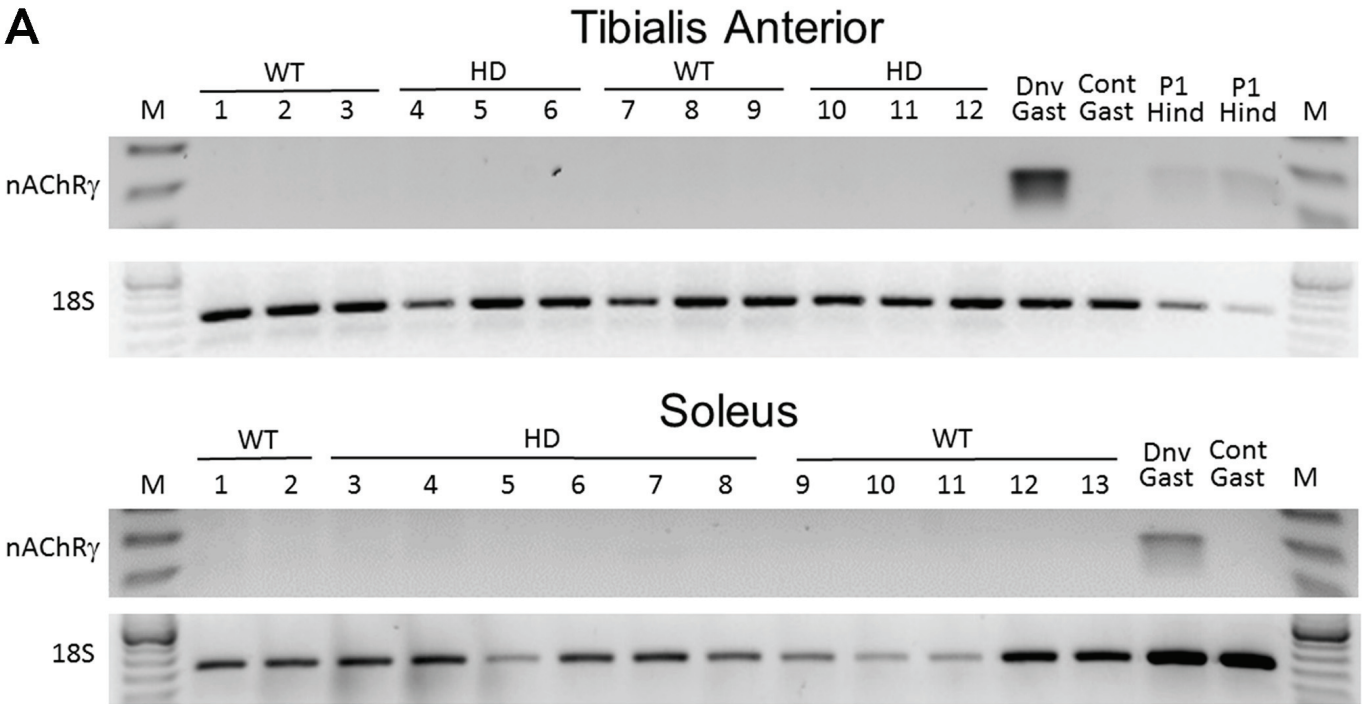


Figure 4

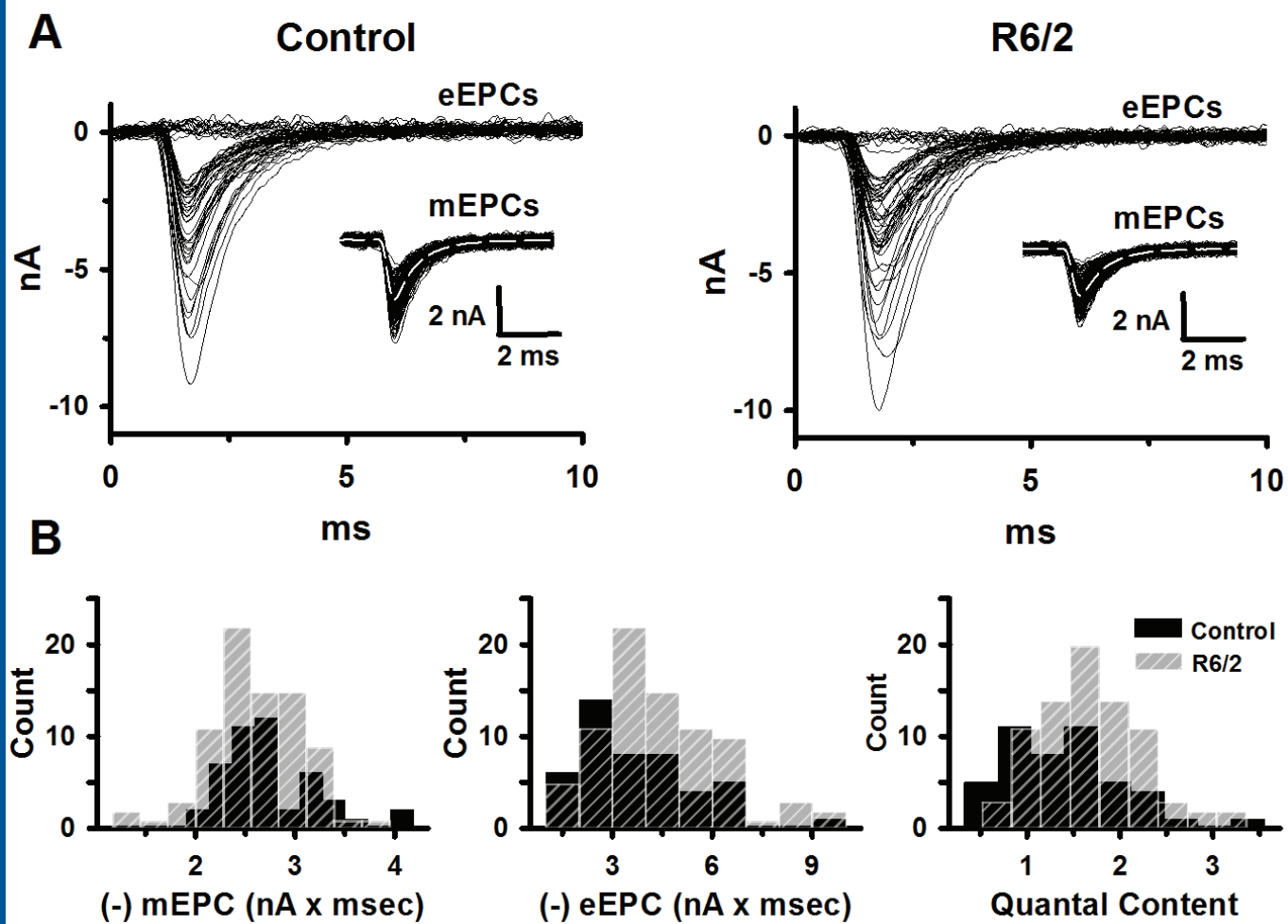


Figure 5

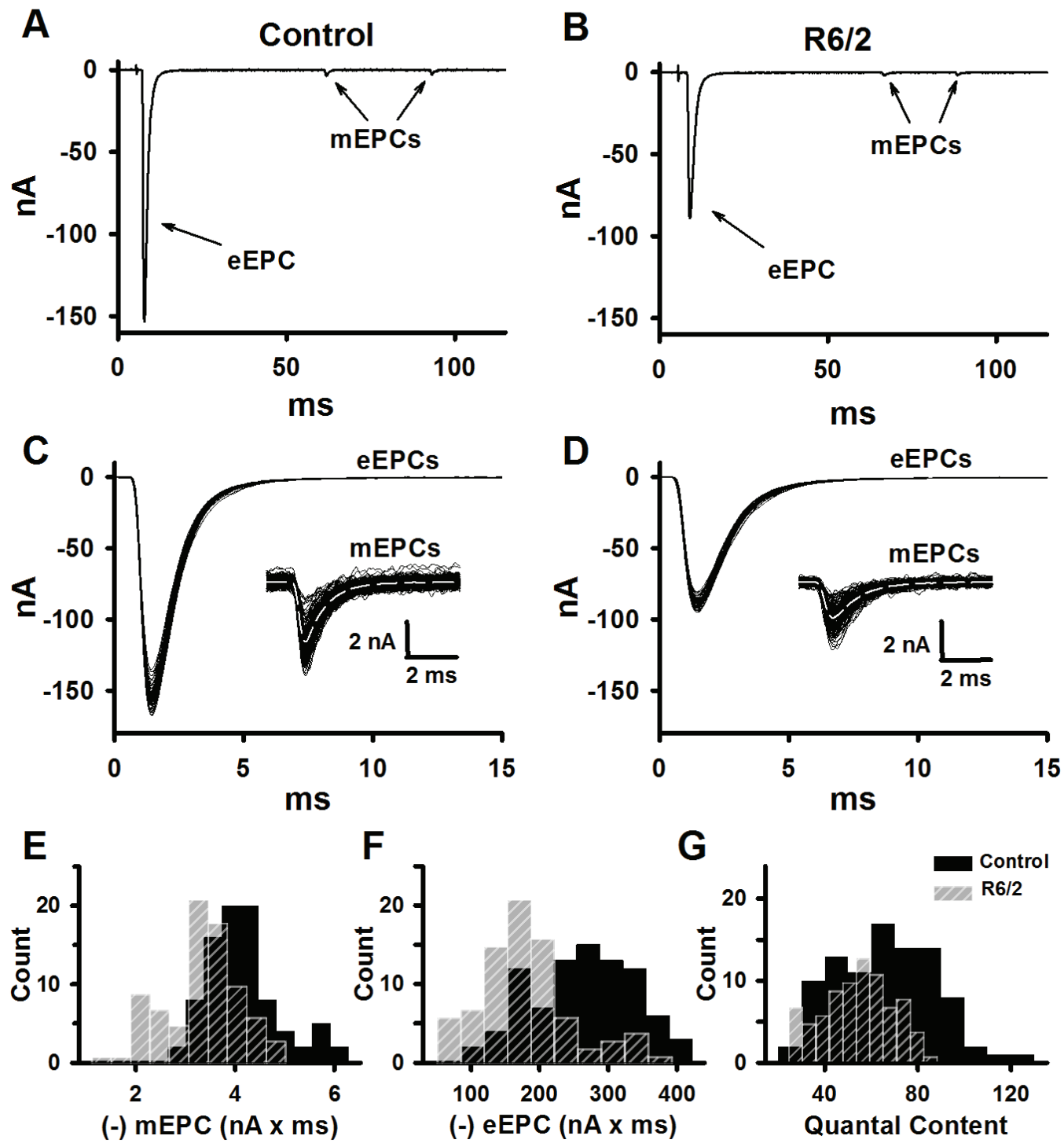
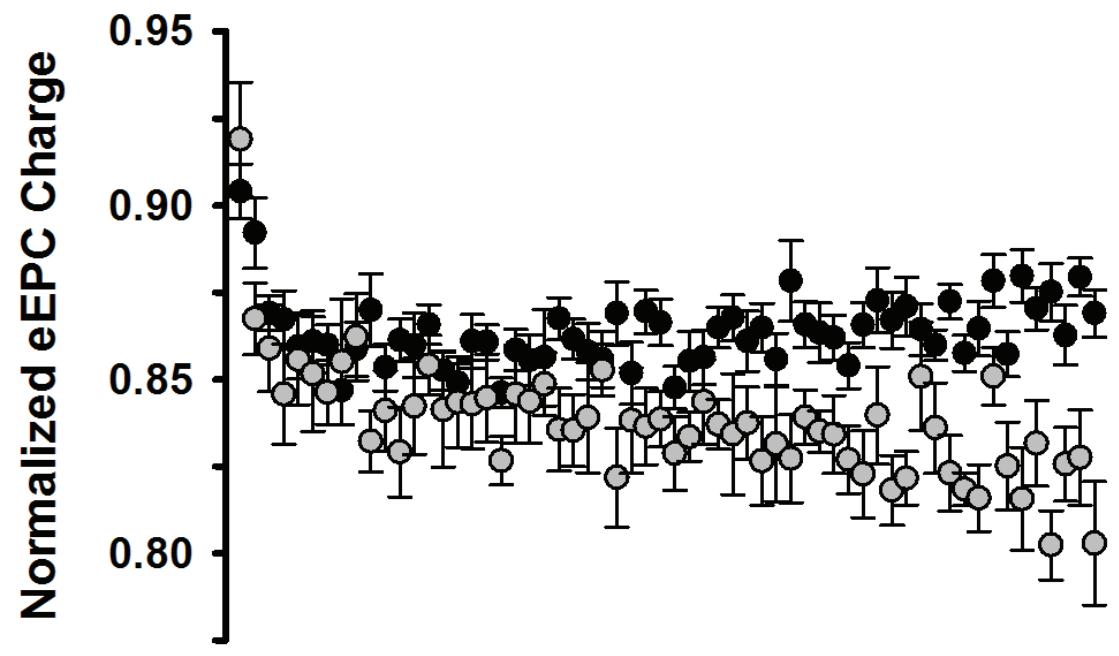


Figure 6

A



B

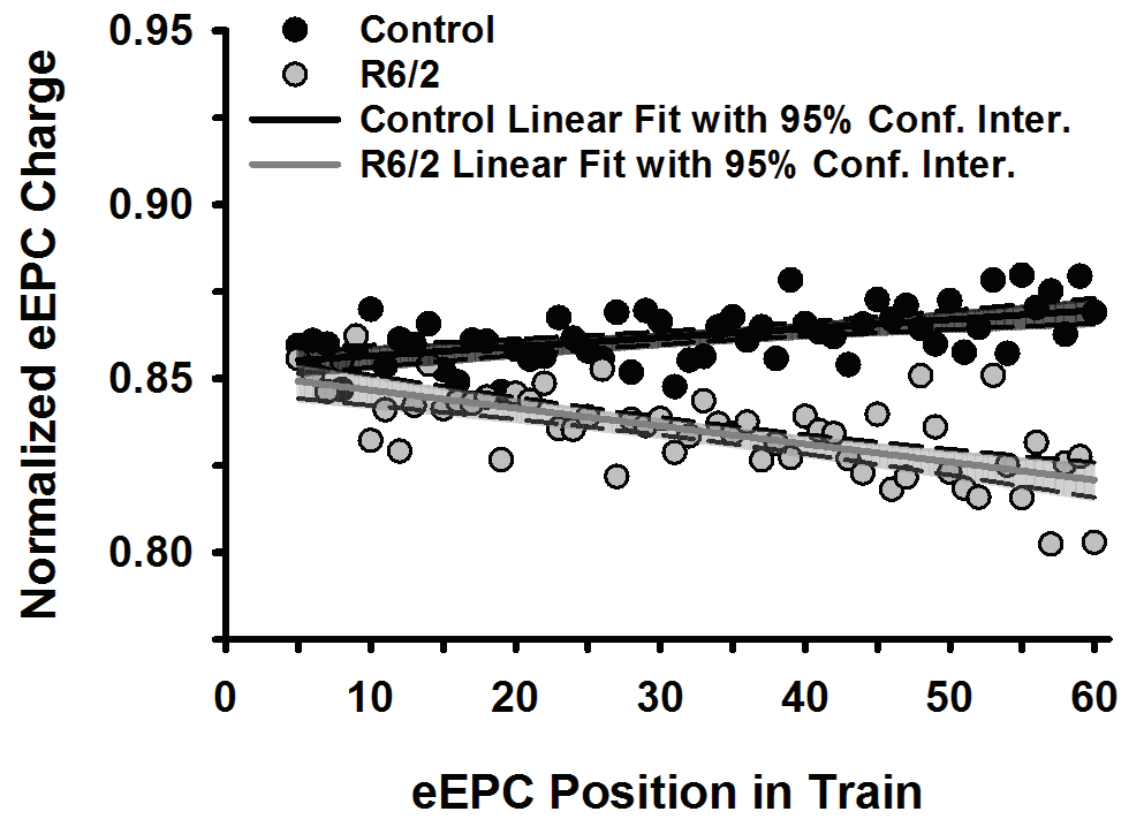


Figure 7

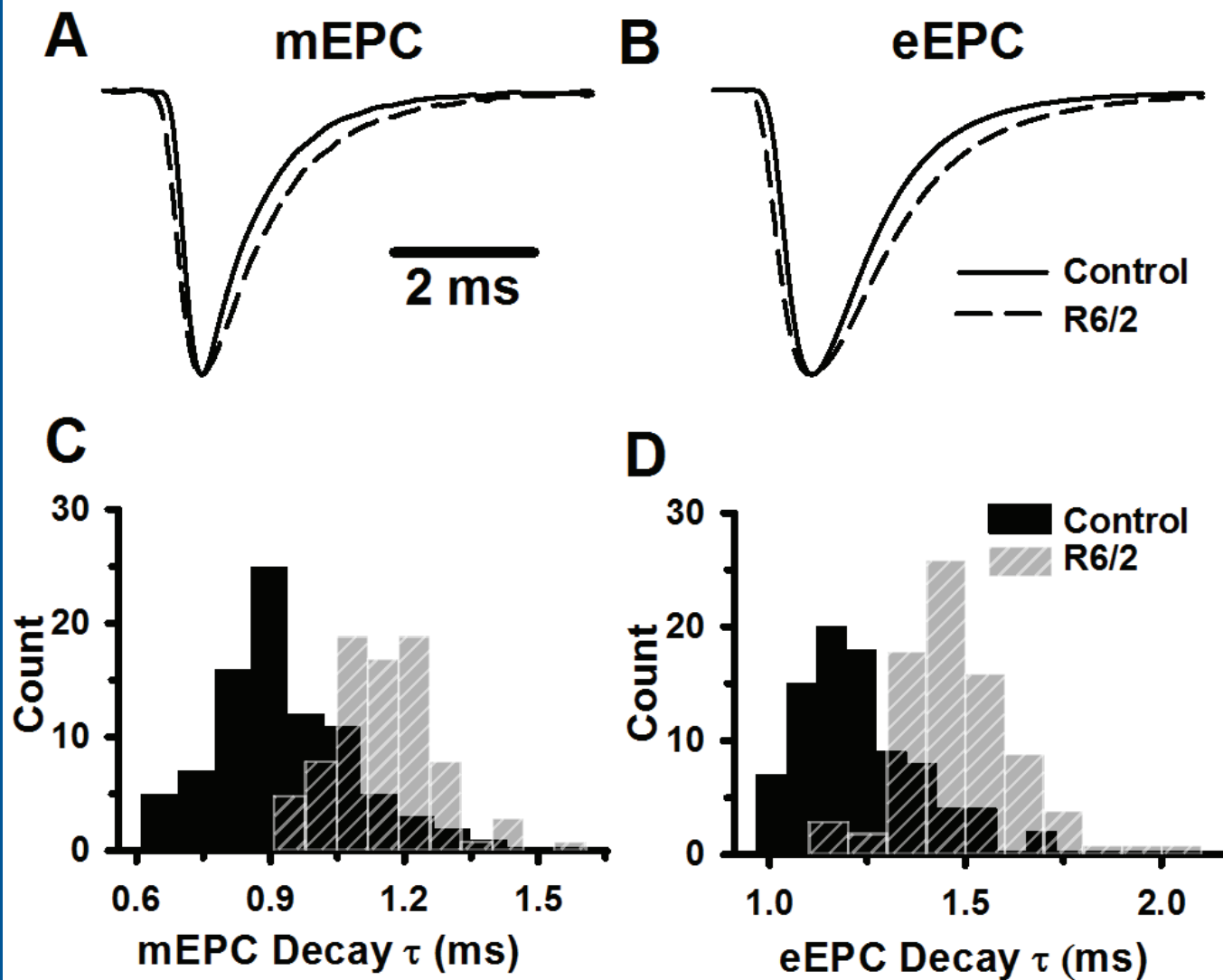


Figure 8

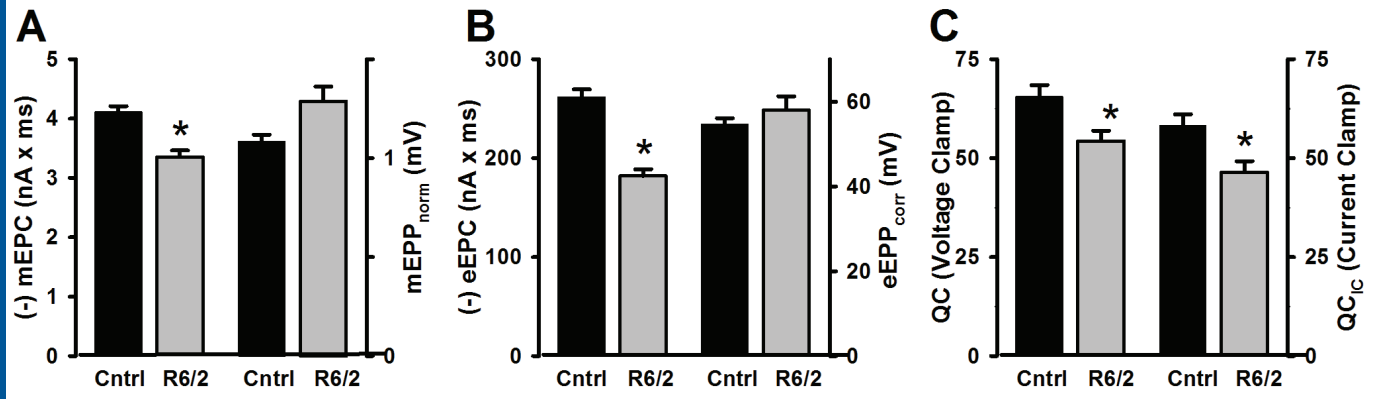


Figure 9

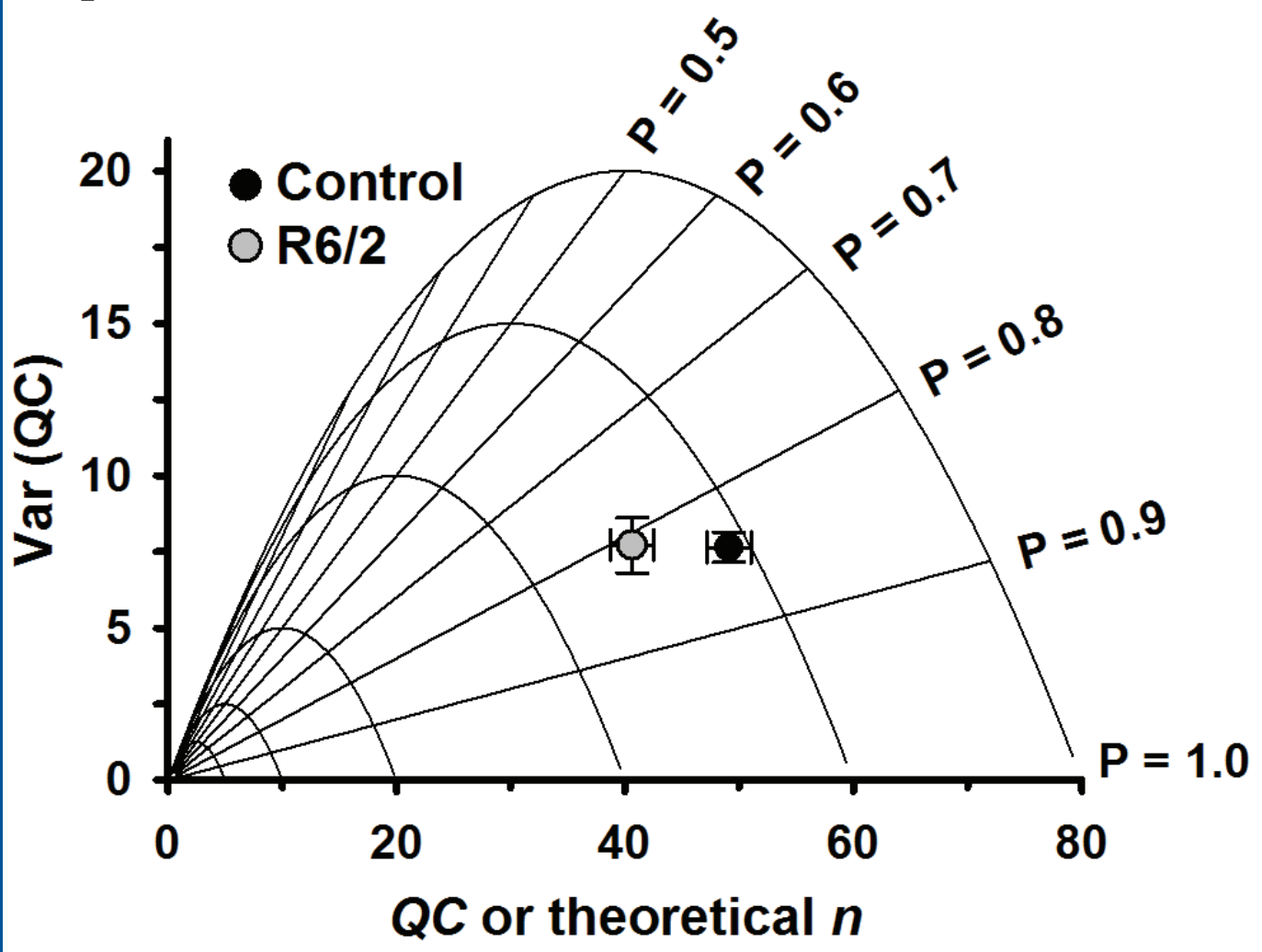


Figure 10

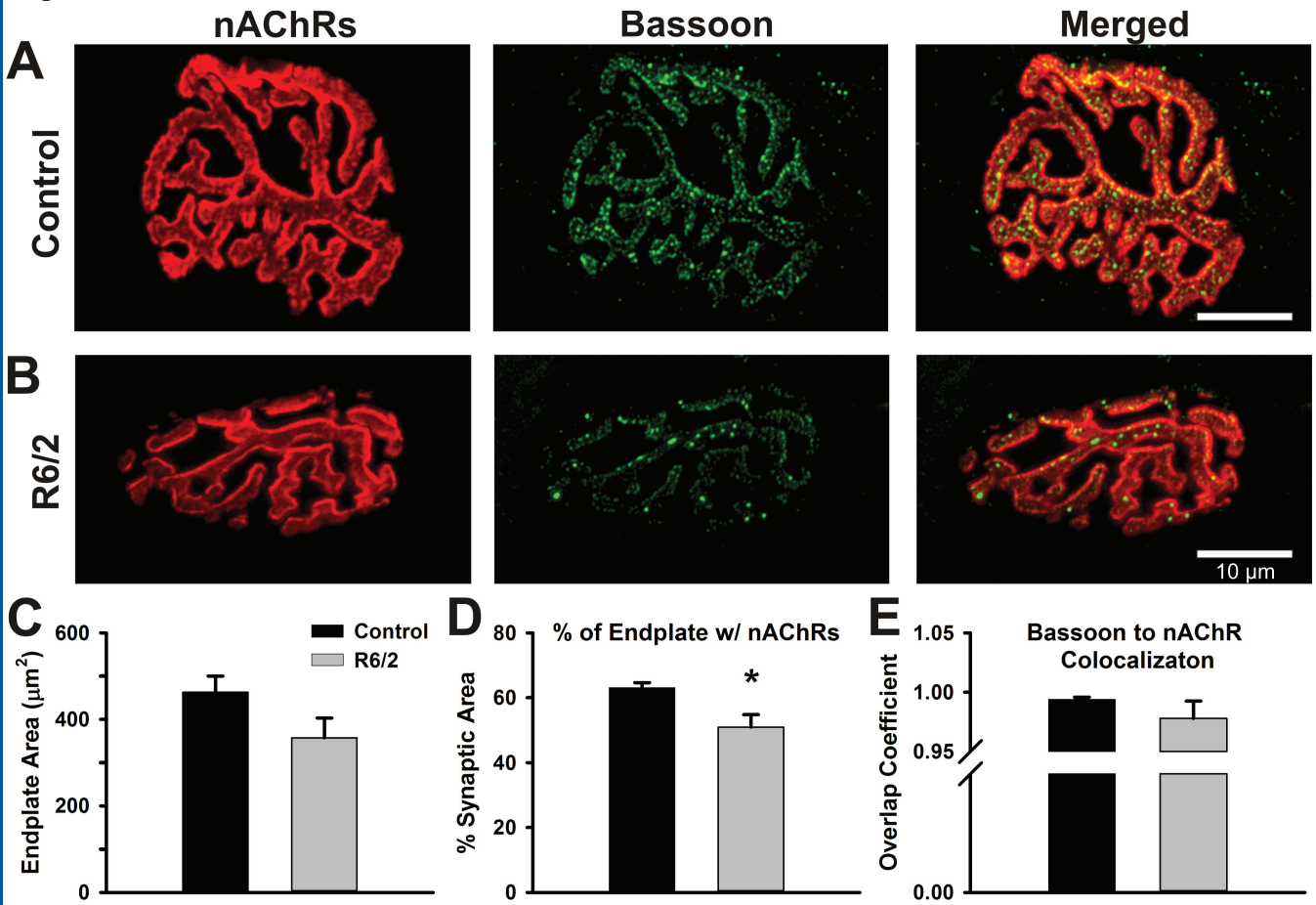


Figure 11

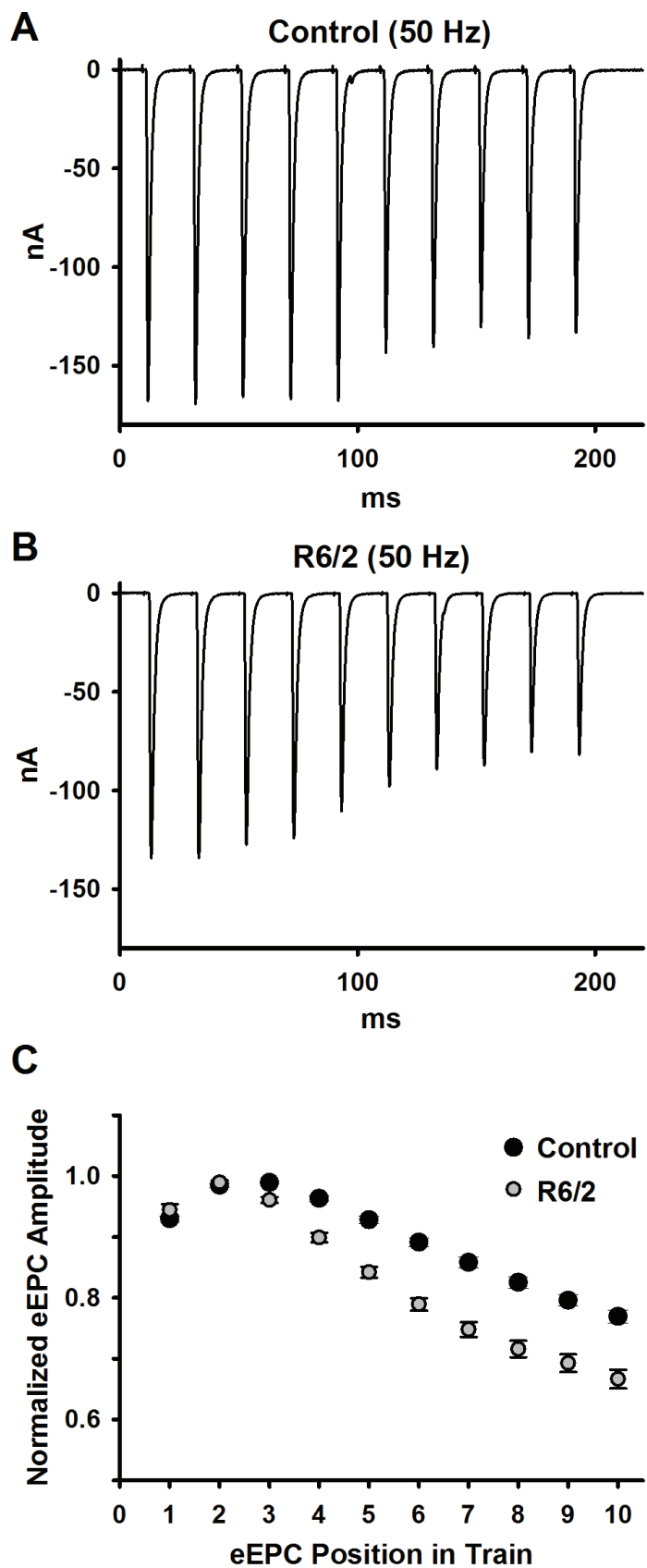


Table 1. mEPC and eEPC properties in physiological calcium conditions.

	mEPC				eEPC			QC
	Charge (pC)	Rise Time (ms)	Decay τ (ms)	Frequency (Hz)	Charge (pC)	Rise Time (ms)	Decay τ (ms)	
Control	-4.1 ± 0.1	0.33 ± 0.01	0.94 ± 0.04	1.5 ± 0.1	-261 ± 8	0.43 ± 0.01	1.24 ± 0.04	65 ± 6
R6/2	$-3.4 \pm 0.1^*$	$0.37 \pm 0.01^*$	$1.16 \pm 0.02^*$	$0.9 \pm 0.1^*$	$-179 \pm 7^*$	$0.47 \pm 0.01^*$	$1.50 \pm 0.04^*$	$54 \pm 5^*$
p-value	1.4×10^{-4}	3.34×10^{-5}	8.36×10^{-4}	1.9×10^{-4}	2.00×10^{-6}	2.11×10^{-4}	2.6×10^{-4}	0.022
t-value	5.06	-5.83	4.16	-4.92	7.47	-4.85	4.75	-2.61
df	15	15	15	15	15	15	15	15

Summary of NMJ data from 81 R6/2 fibers (7 mice) and 87 control fibers (10 age-matched mice). The eEPC rise time was calculated from 10% to 90% of peak. *Indicates a significant difference compared to control. A two-tailed t-test was applied in all measurements.